

An iterative morphological difference product wavelet for weak fault feature extraction in rolling bearing fault diagnosis

Junchao Guo¹, Qingbo He^{1*}, Dong Zhen², Fengshou Gu³, Andrew. D. Ball³

¹State Key Laboratory of Mechanical System and Vibration, Shanghai Jiao Tong University, Shanghai, 200240, China.

²School of Mechanical Engineering, Hebei University of Technology, Tianjin, 300401, China.

³Centre for Efficiency and Performance Engineering, University of Huddersfield, Huddersfield, HD1 3DH, UK.

*Corresponding author. E-mail address: qbhe@sjtu.edu.cn.

Abstract

Weak fault feature extraction is of great significance to the fault diagnosis of rolling bearing. At the early stage of defects, fault features are usually weak and easily submerged in strong background noise, which makes feature information extremely difficult to be excavated. This paper proposes an iterative morphological difference product wavelet (MDPW) to address this issue. In this scheme, firstly, the morphological difference product filter (MDPF) is developed using the combination morphological filter-hat transform operator and difference operator. The MDPF is then incorporated into morphological undecimated wavelet (MUDW) to construct the MDPW, which can achieve noise suppression and fault feature enhancement. Subsequently, the optimal iteration numbers that influence the performance of MDPW is determined using the fault severity indicator (FSI), which effectively extracts periodic impulse related to the failure of rolling bearing. Finally, the fault identification is inferred by the occurrence of fault defect frequencies in the MDPW spectrum with the optimal iteration numbers. The validity of the iterative MDPW is evaluated through numerical simulations and experiment cases. The analysis results demonstrate that the iterative MDPW has higher diagnosis accuracy than existing algorithms (e.g., adaptive single-scale morphological wavelet (ASSMW) and weighted multi-scale morphological wavelet (WMSMW)). This research provides a new perspective for improving the weak fault feature extraction of rolling bearing.

Keywords: Iterative morphological difference product wavelet; Fault severity indicator; Morphological undecimated wavelet; Rolling bearing; Fault diagnosis.

Nomenclature

VMD	Variational mode decomposition
SVD	Singular value decomposition
SR	Stochastic resonance
TQWT	Turntable Q-factor wavelet transform
FFT	Fast fourier transform
MF	Morphological filter
SE	Structural element
MMG	Multi-scale morphological gradient
IMDIF	Improved multi-scale difference filter
LMD	Local mean decomposition
MMSF	Multiscale morphology stationary filter
AMCMFH	Adaptive multi-scale combination morphological filter-hat
AMIDIF	Adaptive multi-scale improved differential filter
MDPF	Morphological difference product filter
MDPO	Morphological difference product operator
MUDW	Morphological undecimated wavelet
MDPW	Morphological difference product wavelet
FSI	Fault severity indicator
$G_{D\&E}$	Gradient filter
$A_{C\&O}$	Average filter
$G_{C\&O}$	Difference filter
BTH	Black top hat
WTH	White top hat
OC	Opening-closing
CO	Closing-opening
$A_{CO\&OC}$	Combination morphological filter based on OC and CO
$G_{CO\&OC}$	Difference filter based on OC and CO
$A_{CO\&OC}H$	Morphological filter-hat transform
MOs	Morphological operators
FFR	Fault feature ratio
FI	Fault indicator
ASSMW	Adaptive single-scale morphological wavelet
WMSMW	Weighted multi-scale morphology wavelet
$A_{CO\&OC}W$	Combination morphological wavelet
$G_{CO\&OC}W$	Difference wavelet
$A_{CO\&OC}HW$	Morphological filter-hat transform wavelet

1. Introduction

Rolling bearings have always played a vital role in modern industries. However, they are susceptible to structural damage due to the interference of complex transmission paths and harsh working environments.¹ Therefore, fault detection of rolling bearing is critical for the safe and stable operation of major equipment.²⁻³ Since vibration signals convey abundant information representing the health status of rolling bearing, the vibration-based methods have been regarded as the most effective and reliable ones for rolling bearing fault detection.⁴⁻⁵ Vibration signals from faulty bearing are normally non-linear and non-stationary, the time-domain and frequency-domain approaches (e.g., time series analysis, fast Fourier transform (FFT), envelope analysis and cepstrum analysis) are difficult to effectively identify fault features. Thus, various advanced signal analysis approaches such as variational mode decomposition (VMD), singular value decomposition (SVD), turntable Q-factor wavelet transform (TQWT) and stochastic resonance (SR) are utilized to extract impulse features to obtain accurate diagnosis results. However, the shortcomings of these methods limit their practical applications. For example, the VMD is a typical non-stationary decomposition method, but it is affected by the balance parameters and the number of modes.⁶⁻⁷ The SVD is a remarkable noise reduction algorithm that can obtain the periodic component of the signal, but its decomposed matrix cannot be explained.⁸⁻⁹ The TQWT can effectively separate fault-related components from sustained oscillatory components, but it is restricted by the choice of Q factor.¹⁰⁻¹¹ The SR is a prominent method for obtaining transient impulses, but its system parameters will affect the denoising effect.¹²⁻¹³ Thus, it is of great significance to explore a remarkable signal processing method to extract the weak fault features of rolling bearing.

As one of the famous time-frequency analysis algorithms, morphological filter (MF) was initially put forward for image analysis by Matheron and Serra in 1987.¹⁴ Recently, MF has been developed into the field of fault detection because it can effectively modify signal details through combining with structural element (SE) when filtering or masking background noise.¹⁵⁻¹⁶ Currently, single-scale MFs have been applied for rolling bearing fault detection.¹⁷⁻¹⁹ However, the impulse features from rolling bearing signals are usually distributed on multiple scales. In addition, single-scale MFs can effectively obtain fault symptoms for certain measurement signal segmentations, but may not be sufficient for other ones. Thence, single-scale MFs may lack completeness in extracting fault features. Hereafter, multi-scale MFs are put forward to analyze the measurement signal and numerous research results are obtained. For example, Li et al.²⁰ designed a multi-scale morphological gradient (MMG) filter, which is used to separate the impact components submerged under background noise and interference information for bearing fault detection. Jiang et al.²¹ developed a hybrid scheme that combines an improved multi-scale difference filter (IMDIF) with local mean decomposition (LMD) for hydraulic pump fault diagnosis. Li et al.²² presented a multiscale morphology stationary filter (MMSF) based on autocorrelation function for rolling bearing fault detection. Although multi-scale MFs are superior to single-scale MFs in impulse

feature extraction, the weighted coefficients in the multi-scale MFs are the identical so that they cannot represent actual features. As a result, the average of the results under all scales may be non-optimal.

To overcome the shortcomings of multi-scale MFs, Yan et al.²³ presented an adaptive multi-scale combination morphological filter-hat (AMCMFH), which is used to remove background noise to obtain fault features from bearing signals. Deng et al.²⁴ put forward an adaptive multi-scale AVG-Hat filter for diagnosing wheel bearing faults. Guo et al.²⁵ proposed an adaptive multi-scale improved differential filter (AMIDIF) to extract impulse features with strong random noise from rolling bearing signals. Although relatively good weighted coefficients are obtained through the aforementioned adaptive multi-scale MFs, their filtering results may not be able to obtain useful fault components. That is, the application of a large weighted coefficient is beneficial to reduce noise, but is not conducive to preserving fault feature information. Conversely, a smaller weighted coefficient is effective for retaining fault information, but is not good for eliminating noise. Thus, adaptive multi-scale MFs have limitations in mining impulse features related to bearing failure. In addition, the weighted coefficients are represented by complex calculation formulas or empirical knowledge, which is not suitable for application in engineering.

Given the above considerations, an iterative morphological difference product filter (MDPF) is proposed in this study, which is defined by the morphological difference product operator (MDPO) and a fixed SE for loop iteration. In addition, the current operation and the next one is continuous in iterative MDPF. The reason is that when a small scale is applied, if the operation is not continuous, there will be random noise components in iterative MDPF filtered signal and a satisfactory noise reduction effect cannot be obtained. On the contrary, if the next operation is executed based on the result of the current one, even if a small-scale operation is used, the residual noise in the measured signal is gradually eliminated by loop operation. This scheme not only solves the problem of calculating the weighted coefficient of adaptive multi-scale MFs, but also enhances the performance of obtaining transient impulse components. However, the application of iterative MDPF in one-dimensional time series is greatly restricted. Morphological undecimated wavelet (MUDW) presented by Zhang et al.²⁶ in 2008 is a multi-resolution signal decomposition algorithm. It not only inherits the ability of traditional MF to retain signal details, but also continues the wavelet multi-resolution characteristics. These advantages have been applied to solve the problem that traditional MFs are restricted in one-dimensional time series by many scholars.²⁷⁻³¹ In view of this, the MUDW method is used to address the limitation of iterative MDPF to enhance weak fault feature extraction.

To summarize, an iterative MDPW is put forward for rolling bearing fault detection. Firstly, the MDPF is presented by the morphological filter-hat transform operator and the difference operator, and merged into MUDW to construct the MDPW. Hereafter, the optimal iteration number of the MDPW is obtained using the fault severity indicator (FSI), which can address the issue of improper selection of weighted coefficients in traditional MMF. The MDPW involving the optimal iteration number is utilized

to obtain periodic impulses from rolling bearing signals. Finally, the fault frequencies are obtained from spectrum of the periodic impulses. The numerical simulations and experimental applications are applied to prove the effectiveness of the iterative MDPW method. Results indicate that the iterative MDPW provides a potential technique for weak fault feature extraction in rolling bearing fault detection. Moreover, compared with the advanced morphological filter algorithms (e.g., ASSMW and WSMW), the proposed MDPW has extremely strong competitiveness in fault detection.

The remainder of the paper is arranged as follows. Section 2, ‘‘Morphological filters’’ elaborates the basic theory of MFs, and analyzes their performance through numerical simulation. Section 3, ‘‘Iterative MDPW method’’ introduces the algorithmic flow of iterative MDPW. Section 4, ‘‘Simulation studies’’ utilizes iterative MDPW on simulated signals and contrasts it with ASSMW and WSMW. Section 5, ‘‘Experiment validation’’ provides measurement signals collected from cylindrical roller bearing to verify the effectiveness of iterative MDPW. Finally, the conclusions of the research work are summarized in section 6 ‘‘Conclusion’’.

2. Morphological filters

2.1 Basic theories of MFs

Supposing the raw signal $f(n)$ and SE $g(m)$ are the functions over a discrete domain $F = (0, 1, \dots, N - 1)$ and $G = (0, 1, \dots, M - 1)$ ($M \leq N$), respectively. The dilation and erosion are defined as:

$$(f \oplus g)(n) = \max\{f(n - m) + g(m)\} \quad (1)$$

$$(f \ominus g)(n) = \min\{f(n + m) - g(m)\} \quad (2)$$

where \oplus is the dilation operator and \ominus is the erosion operator. The morphological gradient ($G_{D\&E}$) is formulated as the difference between erosion and dilation:³²

$$G_{D\&E}(f(n)) = (f \oplus g)(n) - (f \ominus g)(n) \quad (3)$$

The opening and closing operators are expressed as Eq. (4) and Eq. (5), which is established through cascading the dilation and erosion operators:

$$(f \circ g)(n) = (f \ominus g \oplus g)(n) \quad (4)$$

$$(f \bullet g)(n) = (f \oplus g \ominus g)(n) \quad (5)$$

where \circ means the opening operator and \bullet represents the closing operator. Based on these basic morphological operators, the average filter ($A_{C\&O}$) and difference filter ($G_{C\&O}$) between the closing and opening operator are respectively formulated as:²²⁻²³

$$A_{C\&O}(f(n)) = \frac{(f \circ g)(n) + (f \bullet g)(n)}{2} \quad (6)$$

$$\begin{aligned}
G_{c\&o}(f(n)) &= (f \bullet g)(n) - (f \circ g)(n) \\
&= [(f \bullet g)(n) - f(n)] + [f(n) - (f \circ g)(n)] \quad (7) \\
&= BTH(f(n)) + WTH(f(n))
\end{aligned}$$

where $(f \bullet g)(n) - f(n)$ and $f(n) - (f \circ g)(n)$ stand black top-hat (BTH) and white top-hat (WTH), respectively.

The closing-opening (CO) and opening-closing (OC) filters are constructed by cascading the opening and closing operators, which are defined as:

$$CO(n) = (f \bullet g \circ g)(n) \quad (8)$$

$$OC(n) = (f \circ g \bullet g)(n) \quad (9)$$

Based on the combination of CO and OC, the combination morphological filter ($A_{CO\&OC}$) and difference filter ($G_{CO\&OC}$) are defined as:³³⁻³⁴

$$A_{CO\&OC}(f(n)) = \frac{CO(f(n)) + OC(f(n))}{2} = \frac{(f \bullet g \circ g)(n) + (f \circ g \bullet g)(n)}{2} \quad (10)$$

$$G_{CO\&OC}(f(n)) = CO(n) - OC(n) = (f \bullet g \circ g)(n) - (f \circ g \bullet g)(n) \quad (11)$$

Combined with original signal and $A_{CO\&OC}$, an improved MF named the combination morphological filter-hat transform ($A_{CO\&OC}H$) is formulated as:³⁵

$$A_{CO\&OC}H(f(n)) = f(n) - \frac{CO(f(n)) + OC(f(n))}{2} = f(n) - \frac{(f \bullet g \circ g)(n) + (f \circ g \bullet g)(n)}{2} \quad (12)$$

2.2 Extraction impulse properties of MFs

To test the performance of the morphological operators (MOs) in extracting impulses, a typical numerical signal $x(t) = \sin(10\pi t) + n(t)$ is applied in the simulation study as presented in Fig. 1. The numerical signal consists of a sinusoid signal with the frequency of 5 Hz and cyclic impulses $n(t)$ (i.e., a sequence of positive and negative impulses with the same impulses interval of 400 points), and $x(t)$ is obtained using the sampling frequency of 1024 Hz and 1024 data samples. The MOs (e.g., basic operators and MFs) using a flat SE with the length of $L=10$ then are utilized to process the waveform as illustrated in Fig. 1.

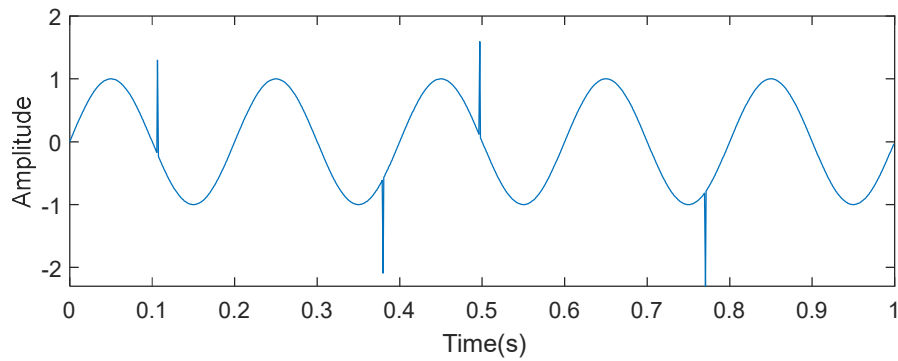
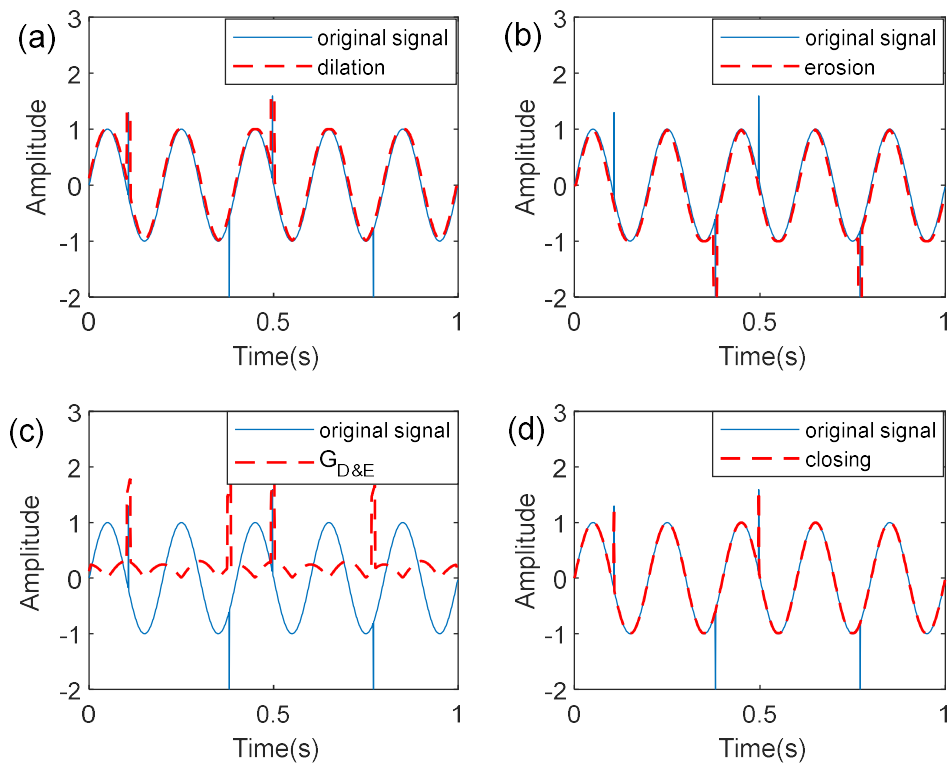


Fig. 1. Waveform of the simulation signal.

Fig. 2 illustrates the filtered results of the MOs. It indicates that the erosion (Fig. 2(b)) and opening (Fig. 2(e)) operators are sensitive to the negative impulses, while the dilation (Fig. 2(a)) and closing (Fig.

2(d)) operators are good at extracting positive impulses. However, the basic operators can only obtain unidirectional impulses, and cannot highlight both the positive and negative impulses. In addition, the results also show that the $G_{D\&E}$ (Fig. 2(c)) can obtain impulses efficiently, but the acquired impulse components are distorted. The OC (Fig. 2(h)), CO (Fig. 2(i)) and $A_{CO\&OC}$ (Fig. 2(j)) cannot effectively acquire positive and negative impulses. The $A_{C\&O}$ (Fig. 2(f)) and $G_{CO\&OC}$ (Fig. 2(k)) are capable of extracting positive and negative impulses, but their impulse amplitudes are weakened. The $G_{C\&O}$ (Fig. 2(g)) and $A_{CO\&OC}H$ (Fig. 2(m)) are able to acquire cyclic impulses simultaneously. Although the direction of the negative impulse extracted by $G_{C\&O}$ is reversed, it will not affect the extraction of fault features.³⁶ Therefore, the simulation results prove that $G_{C\&O}$ and $A_{CO\&OC}H$ are more suitable for extracting bearing signals involving cyclic impulses.



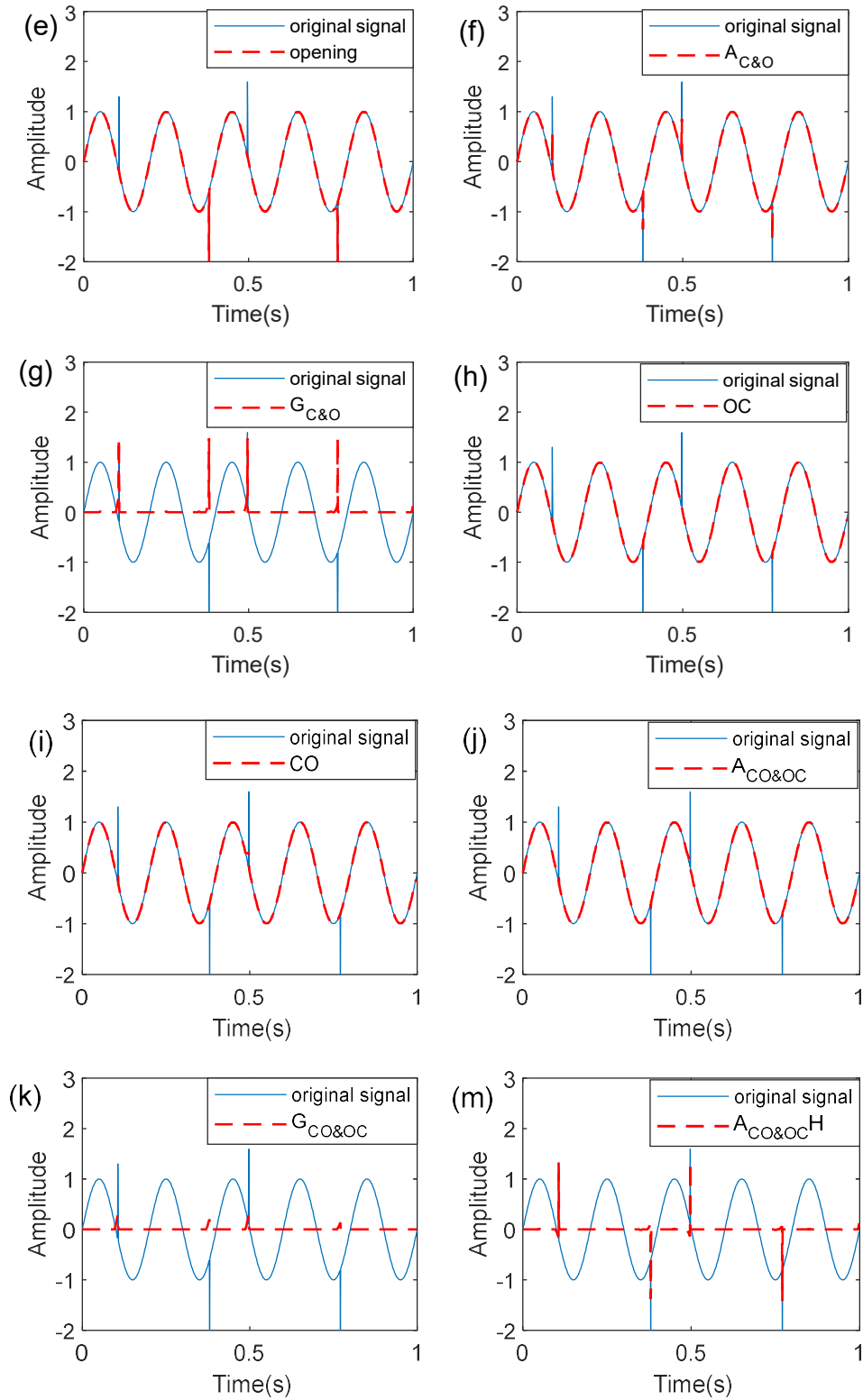


Fig. 2. Filtered results of the MOs: (a) dilation; (b) erosion; (c) $G_{D\&E}$; (d) closing; (e) opening; (f) $A_{C\&O}$; (g) $G_{C\&O}$; (h) OC; (i) CO; (j) $A_{CO\&OC}$; (k) $G_{CO\&OC}$; (m) $A_{CO\&OC}H$.

3. Iterative MDPW method

3.1 MDPW

Considering that $G_{C\&O}$ and $A_{CO\&OC}H$ can effectively obtain cyclic impulses in Section 2.2, a novel morphological filter is proposed, called the morphological difference product filter (MDPF), which is defined as follows:

$$\begin{aligned}
MDPF &= G_{C\&O}(f(n)) \cdot A_{CO\&OC}H(f(n)) \\
&= [(f \bullet g)(n) - (f \circ g)(n)] \cdot [f(n) - \frac{CO(f(n)) + OC(f(n))}{2}] \\
&= [(f \bullet g)(n) - (f \circ g)(n)] \cdot [f(n) - \frac{(f \bullet g \circ g)(n) + (f \circ g \bullet g)(n)}{2}]
\end{aligned} \tag{13}$$

where the filtered result of MDPF is equal to the product of $G_{C\&O}$ and $A_{CO\&OC}H$. If the impulses of the signal are extracted by $G_{C\&O}$ and $A_{CO\&OC}H$, the output amplitude of the MDPF will be larger than the analysis result of its single filter. Morphological undecimated wavelet (MUDW) was an effective nonlinear signal processing method, and its decomposition process is defined as follows. Suppose V_j and W_j are two sets, V_j indicates the signal space at the j th scale and W_j represents the detail space at the j th scale. The analyzed signal is decomposed from j th scale into the $j+1$ th scale and contains two analysis operators. The signal analysis consists of the signal analysis operator $\psi_j^\uparrow: V_j \rightarrow V_{j+1}$ and detail analysis operator $\omega_j^\uparrow: V_j \rightarrow W_{j+1}$. In contrast, the signal synthesis operator $\Psi_j^\downarrow: V_{j+1} \times W_{j+1} \rightarrow V_j$. The above coupled wavelet decomposition structure is depicted in Fig. 3.

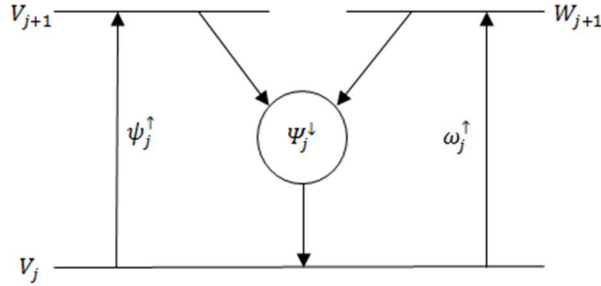


Fig. 3. Structure of coupled wavelet decomposition.

The decomposition scheme needs to meet an integral signal signification, that is, a signal analysis operator $(\psi_j^\uparrow, \omega_j^\uparrow): V_j \rightarrow V_{j+1} \times W_{j+1}$ and a signal synthesis operator $\Psi_j^\downarrow: V_{j+1} \times W_{j+1} \rightarrow V_j$ need to be an opposite process. Thus, the above-mentioned process requires to satisfy the following two conditions:

$$\Psi_j^\downarrow(\psi_j^\uparrow(x), \omega_j^\uparrow(x)) = x \quad \text{if } x \in V_j \tag{14}$$

$$\begin{cases} \psi_j^\uparrow(\Psi_j^\downarrow(x, y)) = x, & \text{if } x \in V_{j+1}, y \in W_{j+1} \\ \omega_j^\uparrow(\Psi_j^\downarrow(x, y)) = y, & \text{if } y \in V_{j+1}, y \in W_{j+1} \end{cases} \tag{15}$$

where x and y indicate the approximate signal and detail signal, respectively. For a signal x_0 , the decomposition is achieved by the Eq. (16):

$$x_0 \rightarrow \{x_1, y_1\} \rightarrow \{x_2, y_2, y_1\} \rightarrow \dots \rightarrow \{x_k, y_k, y_{k-1}, \dots, y_1\} \rightarrow \dots \tag{16}$$

where

$$x_{j+1} = \psi_j^\uparrow(x_j) \in V_{j+1} \quad y_{j+1} = \omega_j^\uparrow(x_j) \in W_{j+1} \tag{17}$$

The x_0 is accurately extracted from x_k and y_k, y_{k-1}, \dots, y_1 by way of the Eq. (18):

$$x_j = \Psi_j^\downarrow(x_{j+1}, y_{j+1}) \quad (18)$$

where $j = k - 1, k - 2, \dots, 0$. The Eq. (18) represents that the decomposition schemes determined by Eq. (16) and Eq. (17) are reversible. Motivated by the MDPF and MUDW, MDPF will be integrated into MUDW to construct the morphological difference product wavelet (MDPW), which is defined as follows:

$$x_{j+1} = \psi_j^\uparrow(x_j) = [(x_j \bullet g)(n) - (x_j \circ g)(n)][x_j(n) - \frac{(x_j \bullet g \circ g)(n) + (x_j \circ g \bullet g)(n)}{2}] \quad (19)$$

$$y_{j+1} = \omega_j^\uparrow(x_j) = x_j - [(x_j \bullet g)(n) - (x_j \circ g)(n)][x_j(n) - \frac{(x_j \bullet g \circ g)(n) + (x_j \circ g \bullet g)(n)}{2}] \quad (20)$$

$$\Psi_j^\downarrow(\psi_j^\uparrow(x_j), \omega_j^\uparrow(x_j)) = \psi_j^\uparrow(x_j) + \omega_j^\uparrow(x_j) = x_j \quad (21)$$

where $x_j \in V_j$, $x_{j+1} \in V_{j+1}$, $y_{j+1} \in W_{j+1}$. The Eq. (19) represents that the signal analysis operator is composed of two parts: $(x_j \bullet g)(n) - (x_j \circ g)(n)$ and $x_j(n) - \frac{(x_j \bullet g \circ g)(n) + (x_j \circ g \bullet g)(n)}{2}$.

3.2 Selection scheme of iteration numbers

Since the decomposition level, structural elements (SE) and iteration numbers have a great influence on the capability analysis of iterative MDPW, it is of great significance to discuss their selection criteria. For the first aspect, fewer decomposition levels may result in too low resolution for accurate identification, but more decomposition levels may lead to excessive calculations. According to Ref [37-38], the decomposition level is set to four to effectively divide the fault frequency band in this study. Therefore, the four approximate signals (x_1, x_2, x_3, x_4) and four detail signals (y_1, y_2, y_3, y_4) are generated as illustrated in Fig 4. Besides, the maximum kurtosis criterion can be applied to find the best MDPW results from four approximate signals.^{36,39} For the second aspect, SE has little effect on the analysis results because the length of SE is given in the iterative MDPW. In addition, according to the Ref [33,40], the SE length is much smaller than the measured signal length, but larger than the narrowband impulse length. Thus, the length of several sampling points is taken as the length of SE in this study.

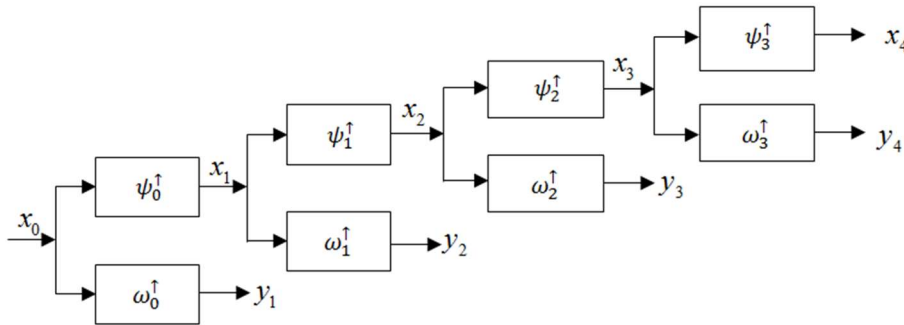


Fig. 4. Four level coupled wavelet decomposition.

It should be pointed out that the iteration numbers are an important part of MDPW to eliminate residual noise and irrelevant components to obtain impulse features. If there are too many iteration

numbers, useful feature information may be lost, while fewer iteration numbers may involve useless feature information. Consequently, it is extremely significant to look for an effective iterative criterion to obtain the optimal iteration numbers of MDPW to retain more useful signal components. Gini index (GI) represents the time domain fault feature indicator and is applied to reveal transient impulses and resist background noise,^{41,42} while fault feature ratio (FFR) indicates the frequency domain fault feature indicator and is used to select the sparsest characteristic fault frequency component. Consequently, combining GI and FFR to construct a novel criterion named FSI, which is a comprehensive fault feature index integrating time domain and frequency domain, which can effectively improve fault features and greatly suppress residual noise and irrelevant components. For a given signal $y(n)$, the fault severity indicator (FSI) is defined as follow:

$$FSI = GI \times FFR$$

$$= \left(1 - 2 \sum_{n=1}^N \frac{y(n)}{\|y\|_1} \left[\frac{N - n - \frac{1}{2}}{N} \right] \right) \times \left(\frac{Y^2(f) + Y^2(2f) + Y^2(3f)}{Y^2} \right) \quad (22)$$

where the vector $y = [y_{(1)}, y_{(2)}, \dots, y_{(N)}]$ and the elements are sorted from smallest to largest, $y_{(1)} \leq y_{(2)} \leq \dots \leq y_{(N)}$. Moreover, $\|y\|_1$ represents the L_1 norm of y , f means the fault defect frequency and Y indicates the amplitudes of the entire frequency spectrum, $Y(f)$, $Y(2f)$ and $Y(3f)$ are amplitudes of the spectrum corresponding to f , $2f$ and $3f$, respectively. If the measured signal has good sparsity characteristics, the value of FSI will be extremely large. In other words, the larger the FSI value, the better the ability of iterative MDPW to extract fault features. Thus, the largest FSI value is used to select the optimal iteration numbers for the MDPW.

3.3 Algorithmic flow of iterative MDPW for bearing fault diagnosis

As mentioned above, an iterative MDPW method for bearing fault detection is developed based on MDPW's good extraction performance for weak fault features and the constructed FSI criteria. The framework of iterative MDPW for rolling bearing fault detection is depicted in Fig. 5, and its diagnostic process is elaborated as follows:

Step1: Collect the measured signal from the rolling bearing using the accelerometer.

Step2: Set the maximum MDPW iteration number $K=50$ and give a fixed flat SE length.

Step3: Conduct the MDPW with a fixed SE length on the vibration signal.

Step4: Calculate the FSI value for each iterative using Eq. (22).

Step5: Estimate whether the termination condition is met or not. If $k > K$, the iteration ends; otherwise, go to step 2 until the optimal iteration number is obtained.

Step6: Perform the MDPW with optimal iteration number to obtain the periodic impulses, and detect the fault defect frequencies from spectrum of the periodic impulses.

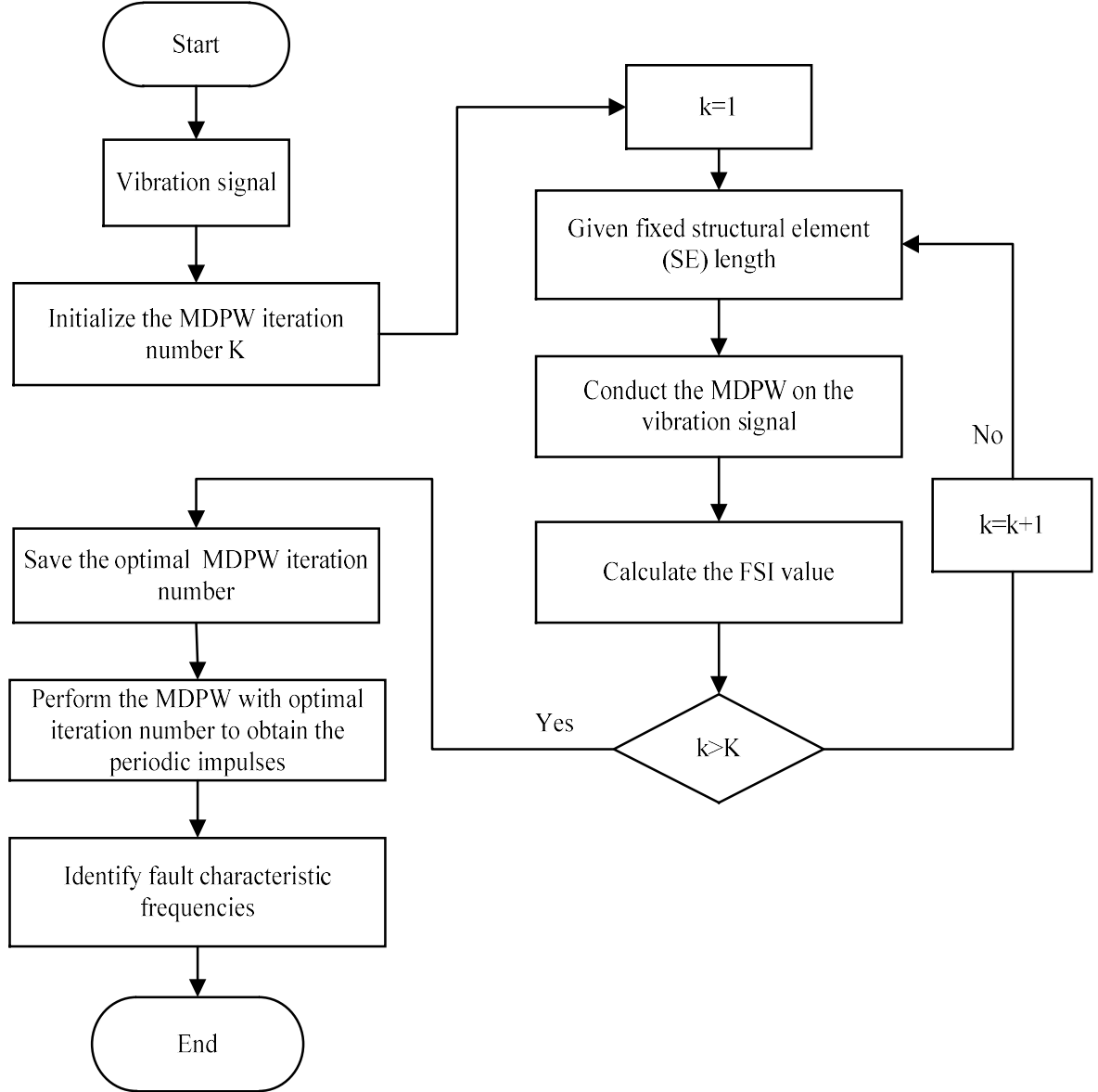


Fig. 5. Framework of the iterative MDPW method.

4. Simulation studies

To verify the performance of the iterative MDPW, the results are compared with adaptive single-scale morphological wavelet (ASSMW) and weighted multi-scale morphological wavelet (WMSMW). The rolling element bearing fault model $x(t)$ with a local fault is expressed as follows:⁴³⁻⁴⁴

$$x(t) = \sum_{n=1}^N B_n e^{-\beta(t-t_i)} \sin(2\pi f_1(t-t_i)) + \sum_{m=1}^M A_m e^{-\alpha(t-mT_p)} \sin(2\pi f_2(t-mT_p)) + n(t) \quad (23)$$

where N denotes the number of impulse responses, B_n indicates the amplitude coefficient, f_1 indicates the nature frequency, equal to 4500 Hz, β means the attenuation factor, equal to 80, and where $t_i = nT_p + \sum_{i=1}^n \tau_i$ in which τ_i indicates the slipping coefficient, which is expressed as $0.01T_p - 0.02T_p$, $T_p = 1/f_o$ stands the period of the impulses, f_o is fault defect frequency, set to 50 Hz, M and A_m

mean the number of random impulses and the amplitude of the m^{th} random impulses, f_2 represents the nature frequency of random impulses, set to 2000 Hz, and α denotes the attenuation factor of random impulses, set to 36, $n(t)$ denotes the white noise added to the simulated signal. Meanwhile, the sampling frequency $f_s=20$ kHz and sampling number $N=80000$. Fig. 6 presents the randomness of fault impulses with different slippage levels (0%, 0.5% and 2%). As displayed in Fig. 6, as more random slippage occurs, the declination from the basic period is larger, so the signal response contains more random components and less periodic components.

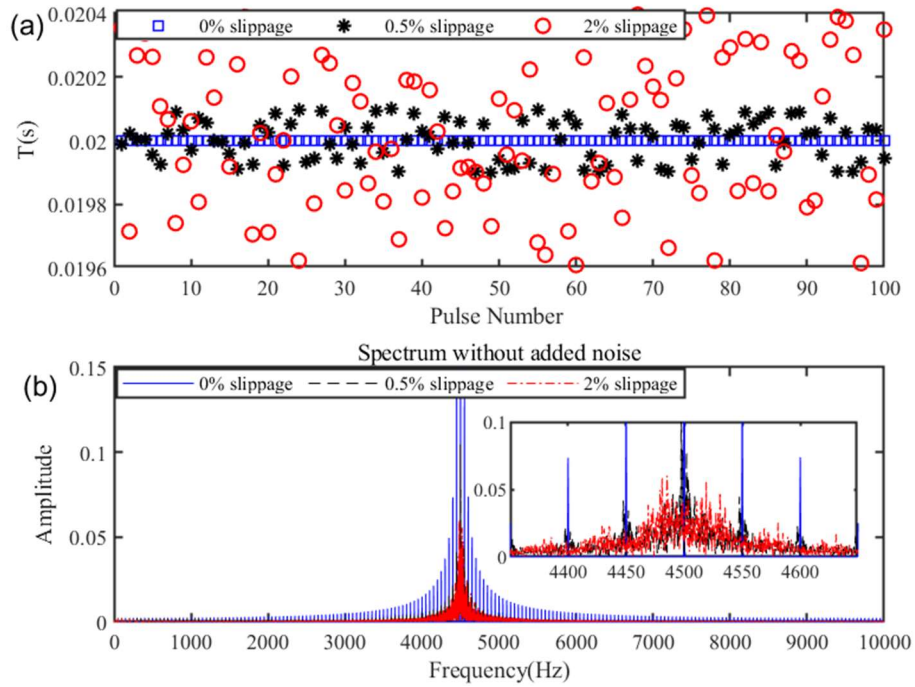


Fig. 6. Simulation case: (a) randomness of fault impulses (b) spectrum.

4.1 Simulation signal with low slippage and low noise

Fig. 7 presents the simulation signal with low slippage and low noise (i.e., random slippage is set to 0.5% and the white noise is generated from a Gaussian distribution with 0 mean and 0.4 standard deviation). The spectrum and envelope spectrum of the mixed signal are described in Fig.7(e) and Fig. 7(f). Obviously, the impulse feature information is completely overwhelmed by the white noise and aperiodic impulsive interference in Fig. 7(e). As displayed in Fig. 7(f), although the fault defect frequencies are discriminated, irrelevant noise is located near the higher harmonics.

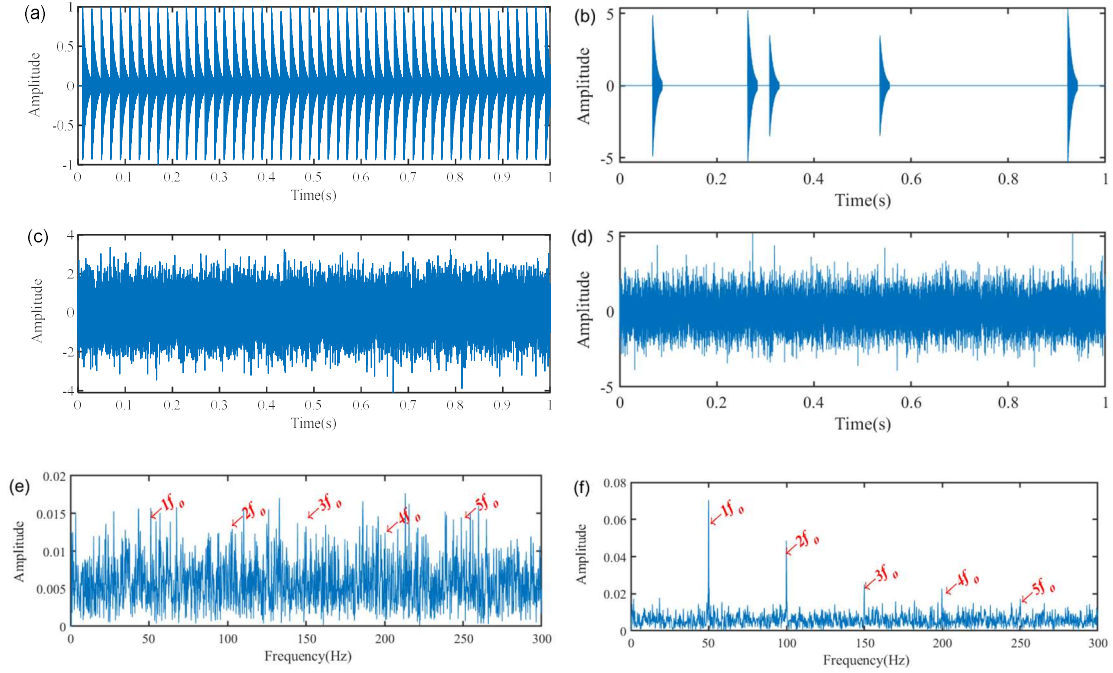


Fig. 7. Simulation signal: (a) periodic impulse signal; (b) aperiodic impulsive interference; (c) white noise; (d) mixed signal; (e) spectrum of the (d); (f) envelope spectrum generated in the frequency band from 4000 Hz to 5000 Hz.

The iterative MDPW then is implemented with a fixed flat SE with length of $L=5$ to analyze the mixed signal as drawn in Fig. 7(d). Subsequently, after placing the iteration number of MDPW in order, the k^{th} iteration MDPW filtered signals is selected to obtain the impulsive components from mixed signal. The whole iteration number of MDPW is K , where $K=50$ and $k=1,2,3,\dots,K$. Thus, there are 50 MDPW filtered signals. After the FSI of 50 MDPW filtered signals are calculated, the FSI values of MDPW filtered signals at each iteration are arranged in sequence, and the process result is plotted in Fig. 8(a). It can be found that the FSI values of MDPW reaches a maximum value when k is 10. At last, the MDPW with 10th are utilized to handle the mixed signal as illustrated in Fig. 8(d), and the detection result is drawn in Fig. 8(c). As illustrated by Fig. 8(c), the background noise is cleaned up and fault defect frequency f_o and its first 5 harmonics are prominent. Thence, the simulation results certificated that the iterative MDPW can accurately extract the fault defect features for rolling bearing fault detection.

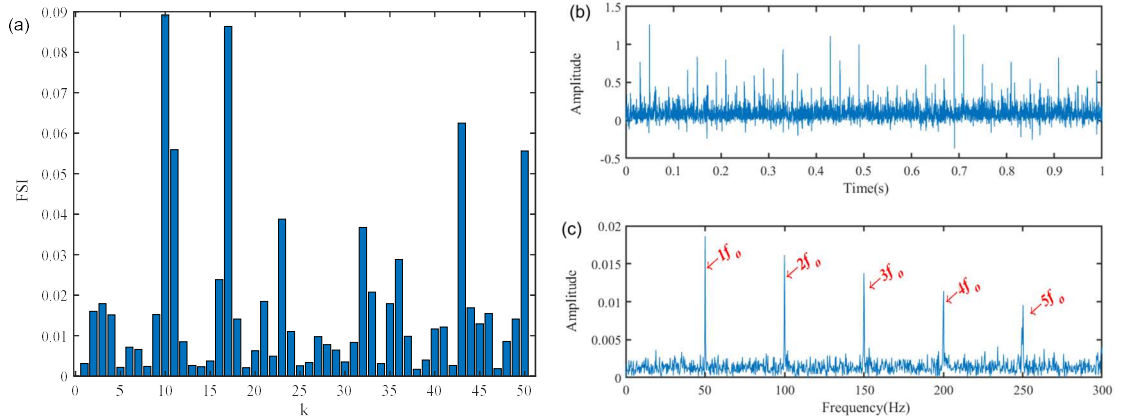


Fig. 8. Detection results of the iterative MDPW: (a) FSI value of MDPW (b) waveform (c) spectrum.

As a comparison, the ASSMW and WMSMW are exploited to handle the same simulated signal as drawn in Fig. 7(d). According to the literature [35], the adaptive single-scale combination morphological filter-hat transform wavelet ($A_{CO\&OC}HW$) consists of the combined morphological filter ($A_{CO\&OC}$) for noise reduction and the morphological white top-hat transform wavelet (WTHW) for feature extraction. A flat SE is used in the $A_{CO\&OC}HW$, and the SE length is optimized by the fault feature ratio (FFR). Fig. 9(a) depicts the FFR values of the filtered signals alongside the SE lengths, and it indicates $L=16$ is the optimized SE length for $A_{CO\&OC}HW$. The detection result of the $A_{CO\&OC}HW$ using the SE length $L=16$ is depicted in Fig. 9(c). It can recognize the fault defect frequencies (i.e., $f_0, 2f_0, 3f_0, 4f_0$ and $5f_0$), but the random noise and noisy frequencies are more than that of Fig. 8(c).

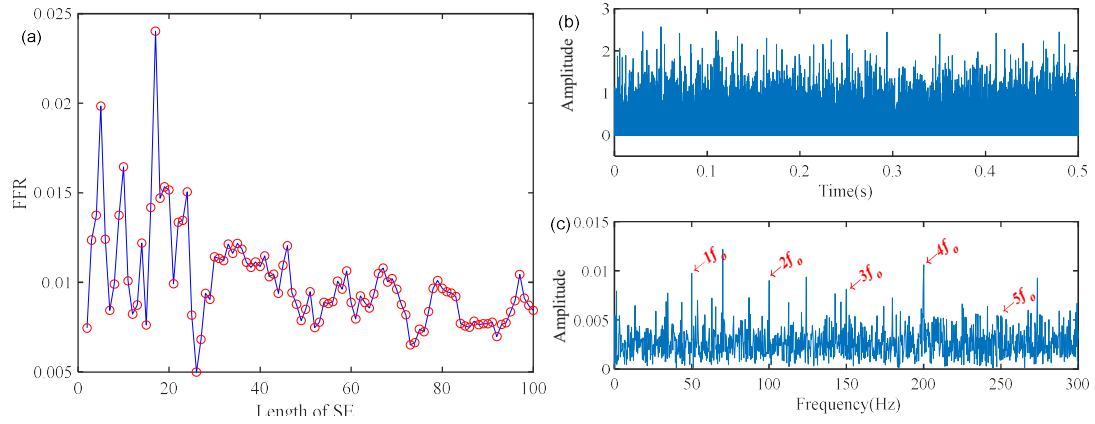


Fig. 9. Detection results of the ASSMW: (a) FFR value of ASSMW under different lengths of SE (b) waveform (c) spectrum.

According to the literature [34], the weighted multi-scale difference morphological wavelet ($G_{CO\&OC}W$) is formed by the $G_{CO\&OC}$ and MUDW. The weighted coefficient using different SE length according to FFR in the $G_{CO\&OC}W$ is illustrated in Fig. 10. The filtered result of the $G_{CO\&OC}W$ is plotted in Fig. 10. As displayed that the $G_{CO\&OC}W$ spectrum, the fault defect frequencies (i.e., $f_0, 2f_0$ and $3f_0$) are observed, but the higher order harmonics (i.e., $4f_0$ and $5f_0$) are not recognized effectively. In addition, it also has background noise and unrelated frequencies. Therefore, the results verified that the iterative MDPW is more accurate for extracting fault features than other morphological filters (i.e., ASSMW and WMSMW).

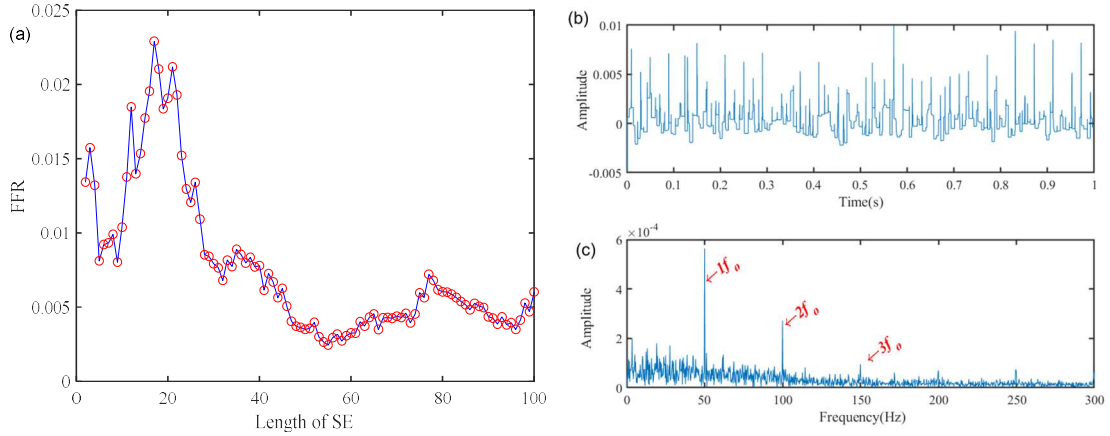


Fig. 10. Detection results of the WSMW: (a) FFR value of WSMW under different lengths of SE (b) waveform (c) spectrum.

4.2 Simulation signal with high slippage and high noise

Fig. 11 illustrates the simulation signal with high slippage and high noise (i.e., random slippage is increased to 2% and white noise is generated from a Gaussian distribution with 0 mean and 0.8 standard deviation). Fig. 11(e) and Fig. 11(f) illustrate the spectrum and envelope spectrum of mixed signal. As displayed in Fig. 11(e) and Fig. 11(f), the fault defect frequency f_o and its first 5 harmonics cannot be recognized because of white noise and aperiodic impulsive interference components.

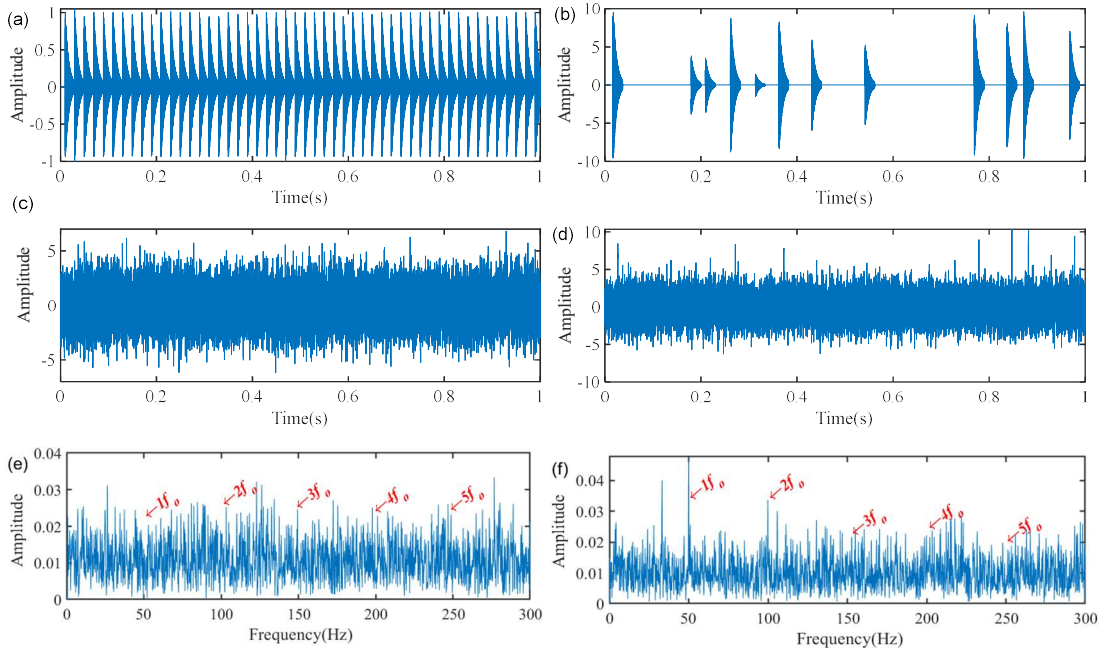


Fig. 11. Simulation signal: (a) periodic impulse signal; (b) aperiodic impulsive interference; (c) white noise; (d) mixed signal; (e) spectrum of the (d); (f) envelope spectrum generated in the frequency band from 4000 Hz to 5000 Hz.

The iterative MDPW is utilized to process the mixed signal. First, the MDPW is implemented with a fixed flat SE with length of $L=5$ to analyze the mixed signal as shown in the Fig. 11(d). Subsequently,

after placing the number of MDPW iterations in order, the FSI of the 50th iterations of MDPW are calculated and the detection result is drawn in Fig. 12(a). As indicated by Fig. 12(a), the FSI illustrates the maximum value when $k=23$. Hence, $k=23$ is chosen as the optimal MDPW iteration numbers. Finally, the MDPW with 23th are used to handle mixed signal as illustrated in Fig. 11(d), and the detection result is drawn in Fig. 12(c). As illustrated by spectrum, the spectral peaks are corresponded to the fault defect frequency f_o and its first 5 harmonics accurately.

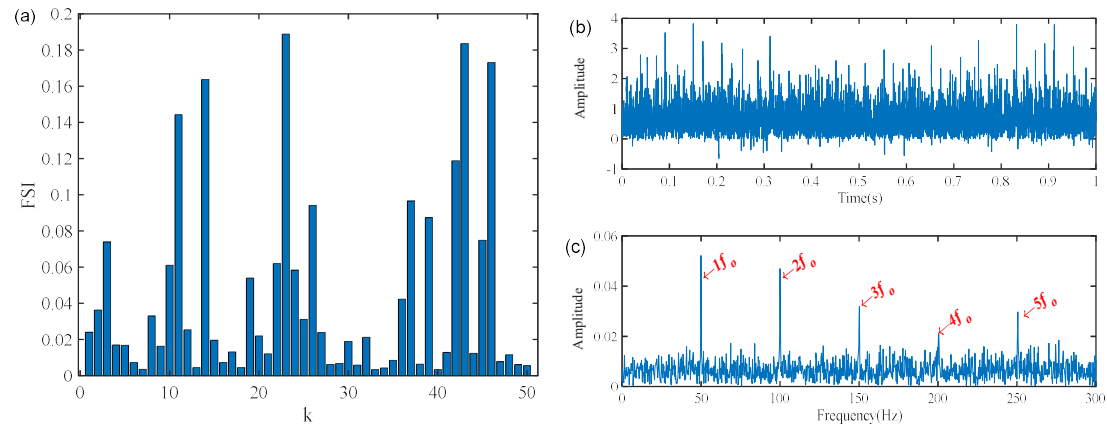


Fig. 12. Detection results of the iterative MDPW: (a) FSI value of MDPW (b) waveform (c) spectrum.

For comparison, the ASSMW and WSMW are used to process the same simulated signal as displayed in Fig. 11(d). The analysis result of ASSMW is shown in Fig. 13(c) using the SE length $L=3$ presented in Fig. 13(a). In Fig. 13(c), although we can discriminate the fault defect frequencies in the spectrum, the irrelevant noise components at higher harmonics that will directly affect the precision of the fault diagnosis results. The analysis result of WSMW is drawn in Fig. 14. As indicated by the WSMW spectrum, the fault defect frequencies (i.e., f_o and $2f_o$) are observed, but the energy of the background noise and interference components is still high in higher order harmonics. Consequently, the comparison analysis demonstrates that the iterative MDPW is better than the ASSMW and WSMW.

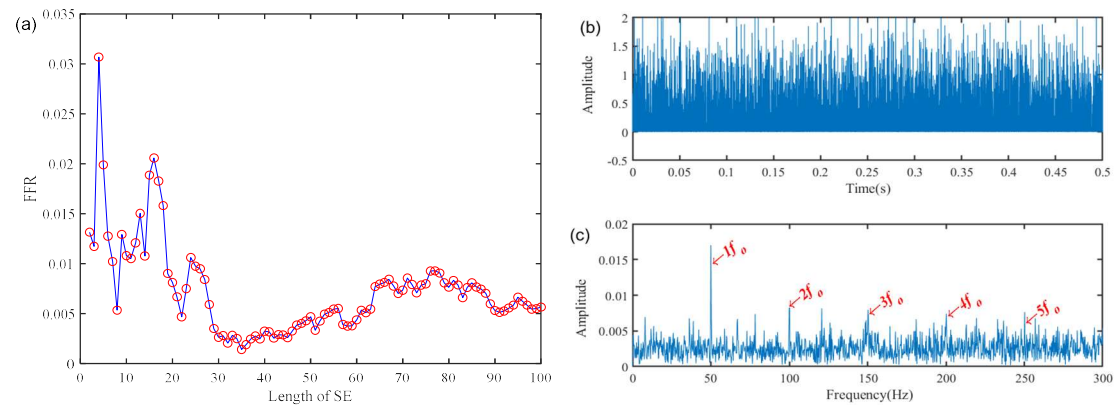


Fig. 13. Detection results of the ASSMW: (a) FFR value of ASSMW under different lengths of SE (b) waveform (c) spectrum.

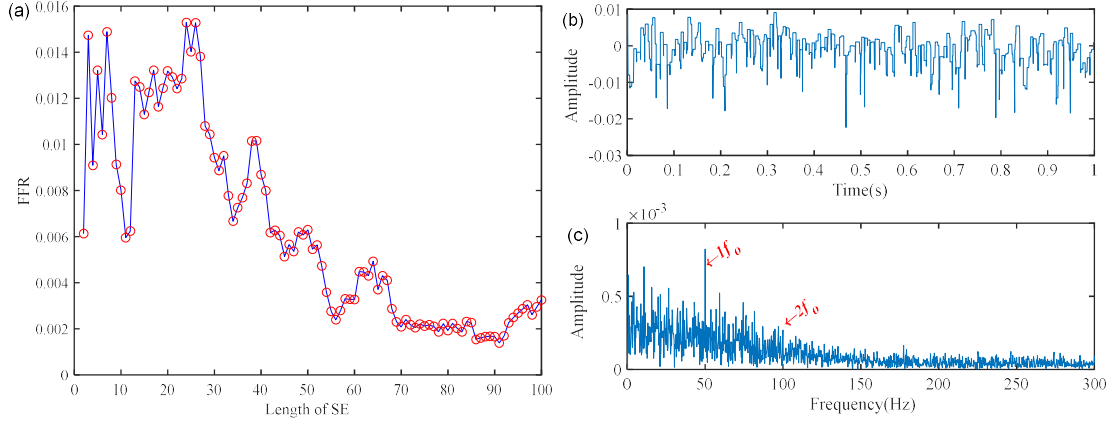


Fig. 14. Detection results of the WSMW: (a) FFR value of WSMW under different lengths of SE (b) waveform (c) spectrum.

4.3 Performance analysis and calculation efficiency

The performance of iterative MDPW on the simulated signal with different white noise standard deviations is also tested. The fault Indicator (FI) is employed to quantify the performance of above-mentioned methods, which is defined as (unit: dB):

$$FI = 10 \log_{10} \left(\frac{P}{\bar{P} - P} \right) \quad (24)$$

where \bar{P} means overall peak value of the signal in the selected frequency band (0-300Hz), P represents the peak value of fault defect frequencies. The FI of three methods is depicted in Fig. 15, where standard deviations vary from 0 to 1, with the increases of 0.2. For each standard deviation, the FI of the iterative MDPW is larger than ASSMW and WSMW. Moreover, as the standard deviation increases, the FI of the iterative MDPW is reduced. The FI of the iterative MDPW is reduced by 13.769 from 19.860 to 6.091 when standard deviations are increased from 0 to 1. In addition, to highlight the advantage of the FSI in selecting the optimal iteration numbers for iterative MDPW, we utilized the GI and FFR to demonstrate the superiority of the proposed FSI criterion. Fig. 16 presents the FI obtained by iterative MDPW using FSI, GI, and FFR. As illustrated in Fig. 16, the FI obtained by using the FSI to select the optimal iteration numbers of iterative MDPW is higher than GI and FFR under different standard deviations.

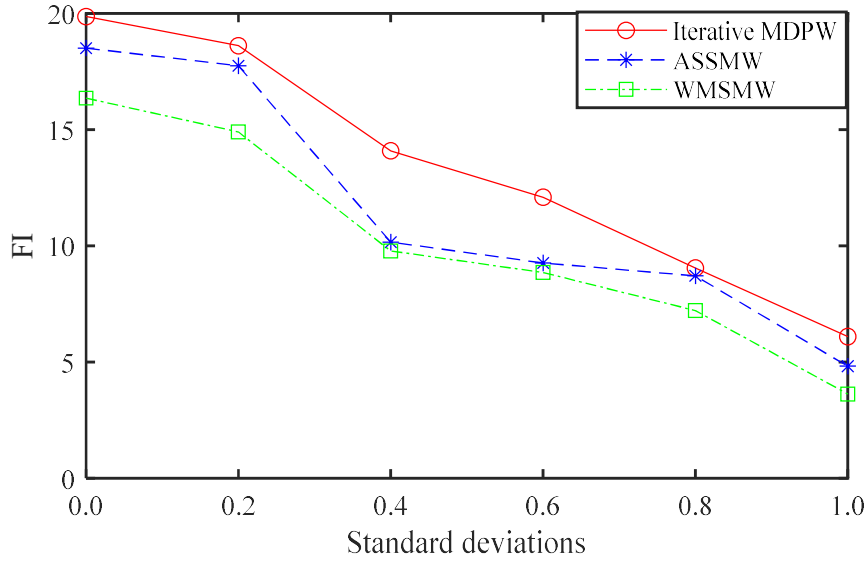


Fig. 15. FI of three methods under different standard deviations.

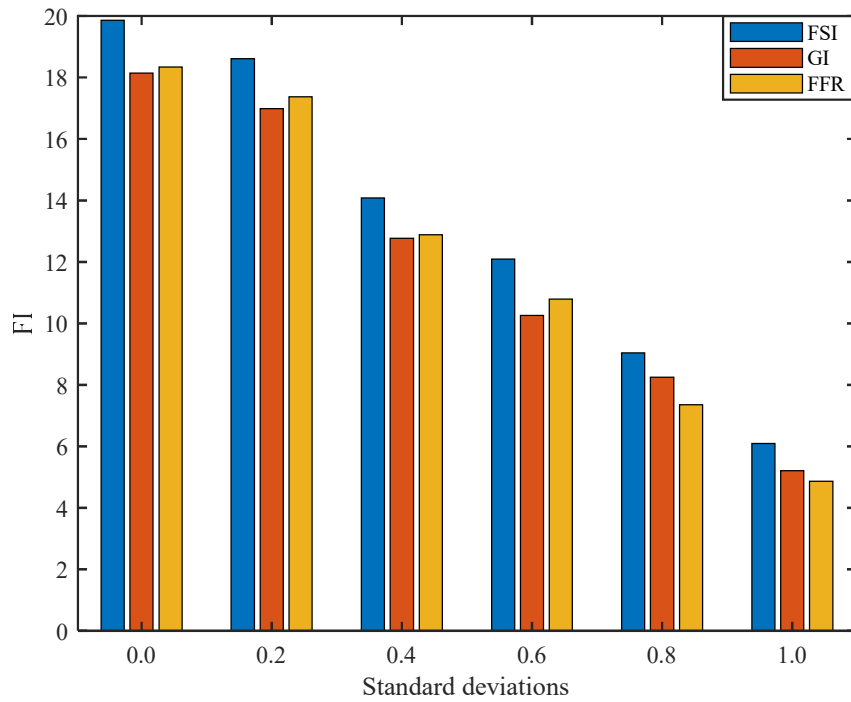


Fig. 16. FI obtained by iterative MDPW using FSI, GI, and FFR under different standard deviations.

In order to further assess the calculation cost of the three methods (e.g., iterative MDPW, ASSMW and WMSMW), they are tested for the CPU time on a laptop computer (i5-4210U processor 2.4 GHz). Fig. 17 presents the CPU time of iterative MDPW, ASSMW and WMSMW. As displayed in Fig. 17, the computational efficiency of iterative MDPW is higher than that of ASSMW and WMSMW. Consequently, the comparison results certificated that the fault diagnosis performance of iterative MDPW is superior to that of ASSMW and WMSMW.

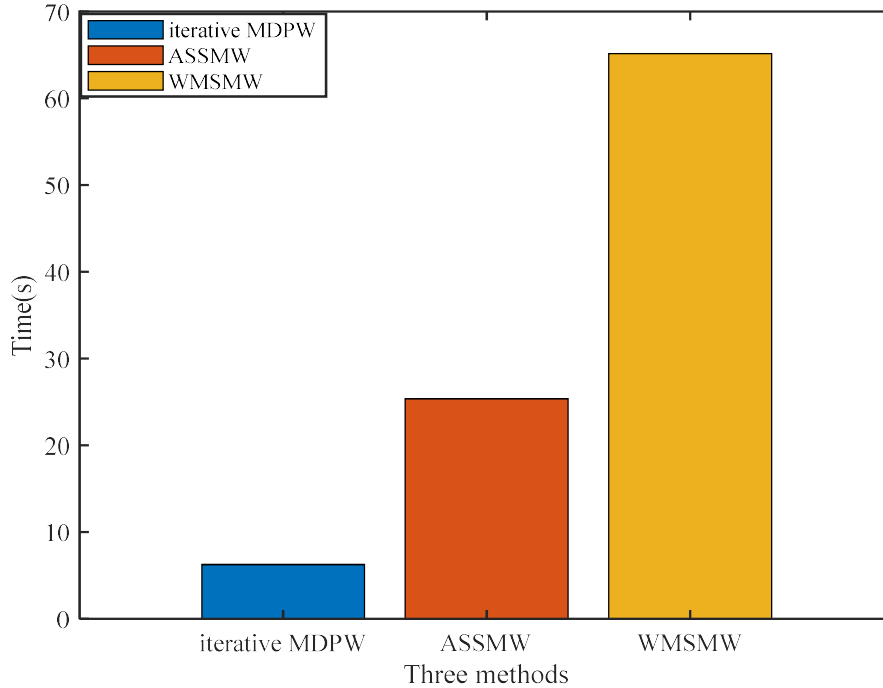


Fig. 17. Calculation time of three methods for simulation studies.

5. Experiments validation

In this section, the iterative MDPW is utilized to handle the vibration signals of cylindrical roller bearing to verify its effectiveness. The test facility of cylindrical roller bearing is drawn in Fig. 18, which consists of four main components: a motor, two bearing houses, three flexible type couplings and a DC generator. In this test, the shaft was running at 1456 rpm. An acceleration sensor is installed on the bearing house to obtain the measurement signals of the cylindrical roller bearing. The inner race and outer race of cylindrical roller bearing have slight defects and are made by electrical discharge machining, as illustrated in Fig. 19. The sampling frequency of data acquisition was 71428 Hz and the data length was 300000. The structure parameters and fault defect frequencies of the cylindrical roller bearing are listed in Tables 1.

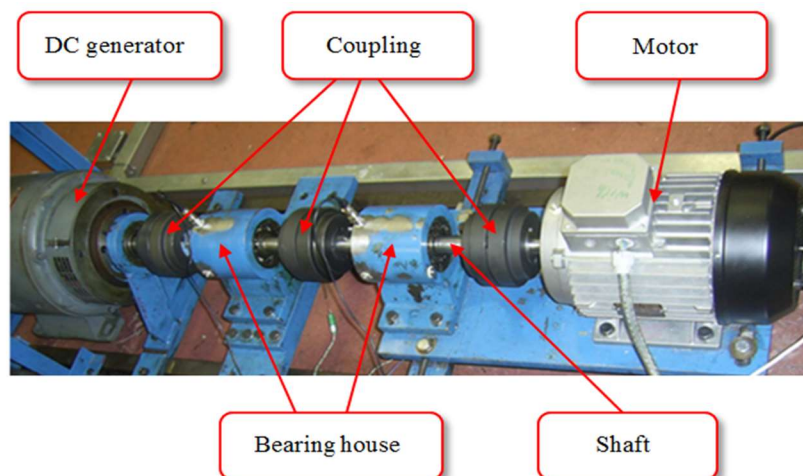


Fig. 18. The test facility of cylindrical roller bearing.

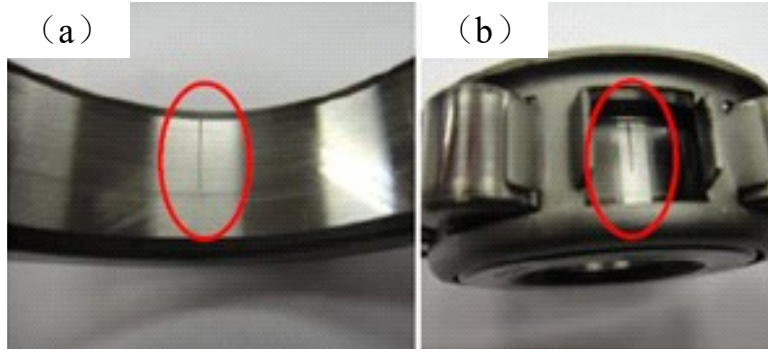


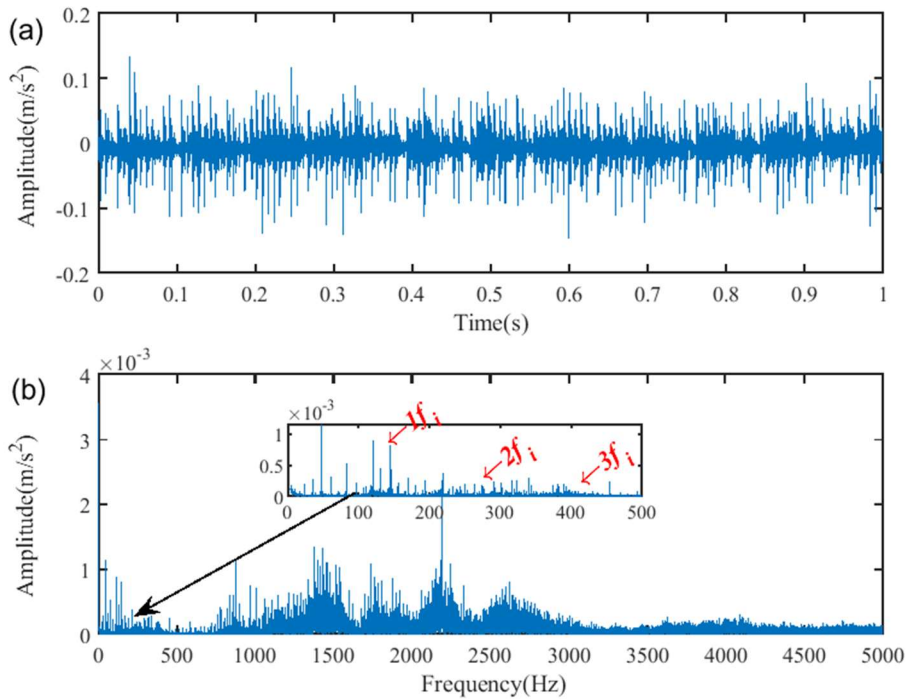
Fig. 19. The cylindrical roller bearing with small defect: (a) inner race; (b) outer race.

Table 1. Structure parameters and fault defect frequencies of the cylindrical roller bearing.

Bearing designation	Ball numbers	Pitch Diameter	Ball Number	Contact Angle
	d (mm)	D_m (mm)	z	β
	14	59	9	0°
N406	f_o	f_i	f_b	f_c
	83.3	135.1	48.3	9.3

5.1 Fault diagnosis for an inner race fault

The waveform, spectrum and envelope spectrum of the cylindrical roller bearing with inner race fault are depicted in Fig. 20. The impulse components cannot be observed in Fig. 20(a), and it is also not sufficient to obtain feature information related to the defective inner race bearing in Fig. 20(b). From Fig. 20(c), the fault defect frequencies are identified, but the residual noise and unrelated frequencies are in the higher harmonics.



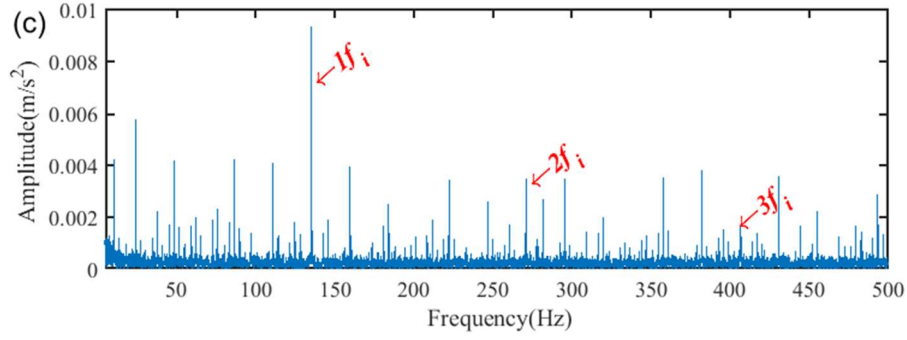


Fig. 20. Cylindrical roller bearing with inner race fault: (a) waveform; (b) spectrum; (c) envelope spectrum generated in the frequency band from 1000 Hz to 3000 Hz.

The iterative MDPW is then utilized to process the cylindrical roller inner race bearing vibration signal. First, the MDPW is implemented using a fixed flat SE with length of $L=5$ to handle the measured signal as displayed in Fig. 20(a). Then, by putting the number of MDPW iterations in order, the FSI of the 50th iterations of MDPW are calculated, and the maximum FSI value appears at $k=15$. Thus, $k=15$ is selected as the optimal MDPW iteration numbers. Finally, the MDPW with 15th are applied to handle the measured signal, and the detection result is depicted in Fig. 21. The spectral peaks corresponding to the fault defect frequency f_i and its first 3 harmonics are enhanced obviously.

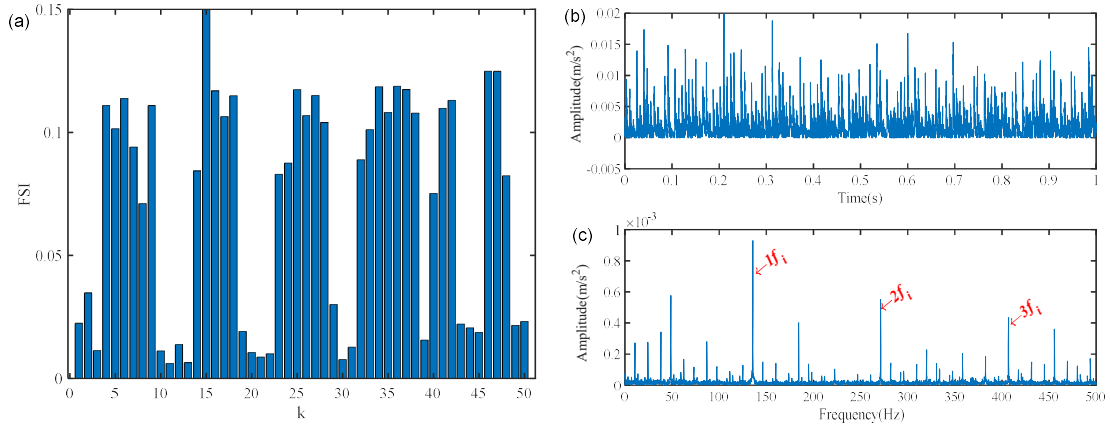


Fig. 21. Detection results of the iterative MDPW: (a) FSI value of MDPW (b) waveform (c) spectrum.

For comparison, the ASSMW and WSMW are used to process defective inner race bearing vibration signal as drawn in Fig. 20(a). Fig. 22 depicts the process result by ASSMW with the length of $L=16$. In Fig. 22(c), although the fault defect frequency f_i and its first 3 harmonics can be recognized in the spectrum, the residual noise and unrelated frequencies are in the higher harmonics. The analysis result by WSMW is presented in Fig. 23. The fault defect frequency f_i and its harmonics (i.e., $2f_i$ and $3f_i$) are detected, but their amplitude is lower than that of MDPW as shown in Fig. 21. Moreover, it has a lot of random noise and uncorrelated frequency components at low frequencies. Therefore, the results reveal that the iterative MDPW is more accurate for obtaining fault features than other morphological filters (i.e., ASSMW and WSMW). Consequently, the experimental results of the cylindrical roller bearing inner fault indicate that the iterative MDPW is better for obtaining fault feature

information from background noise and interference frequencies.

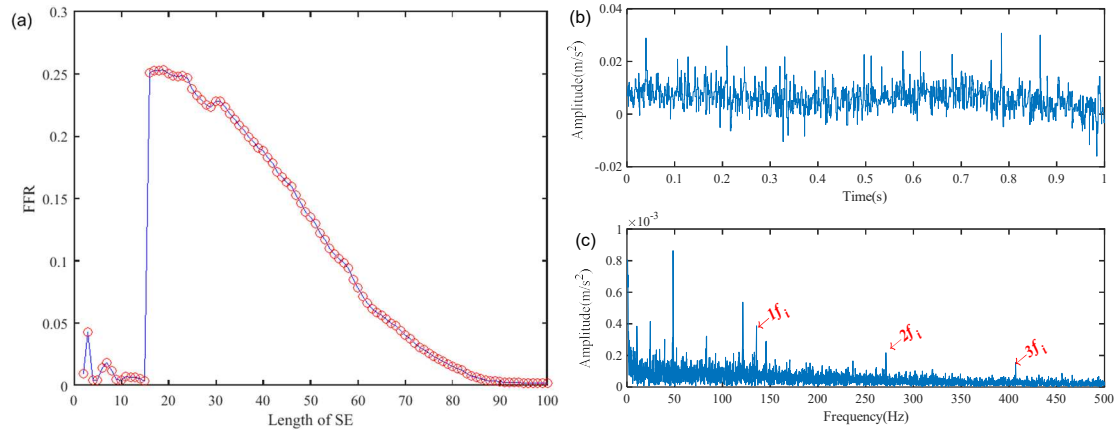


Fig. 22. Detection results of the ASSMW: (a) FFR value of ASSMW under different lengths of SE (b) waveform (c) spectrum.

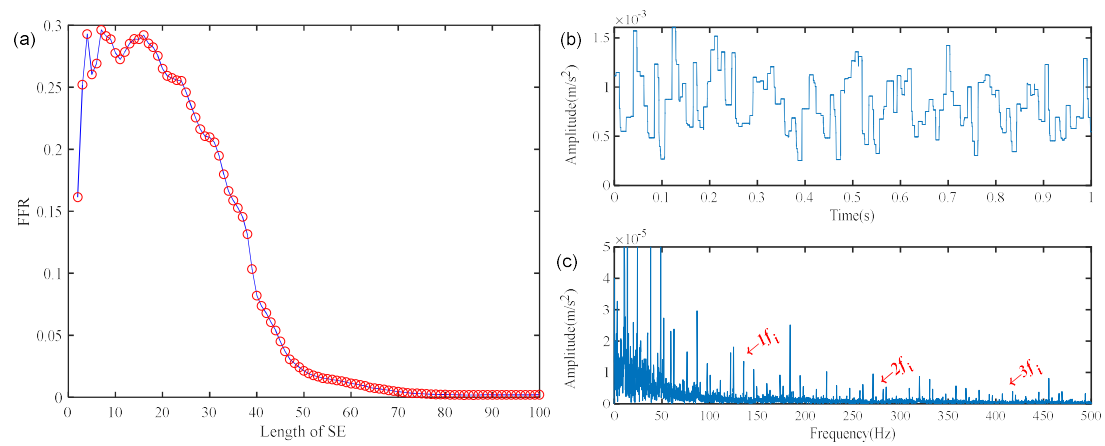


Fig. 23. Detection results of the WMSMW: (a) FFR value of WMSMW under different lengths of SE (b) waveform (c) spectrum.

5.2 Fault diagnosis for an outer race fault

Fig. 24 displays the waveform, spectrum and envelope spectrum of the cylindrical roller bearing with outer race fault. It is found that there are no obvious impulses in Fig. 24(a), and the fault defect frequencies associated with the cylindrical roller bearing outer race fault are not obtained in the spectrum as illustrated in Fig. 24(b). In Fig. 24(c), although the fault defect frequencies are recognized, the residual noise and unrelated frequencies are in the higher harmonics.

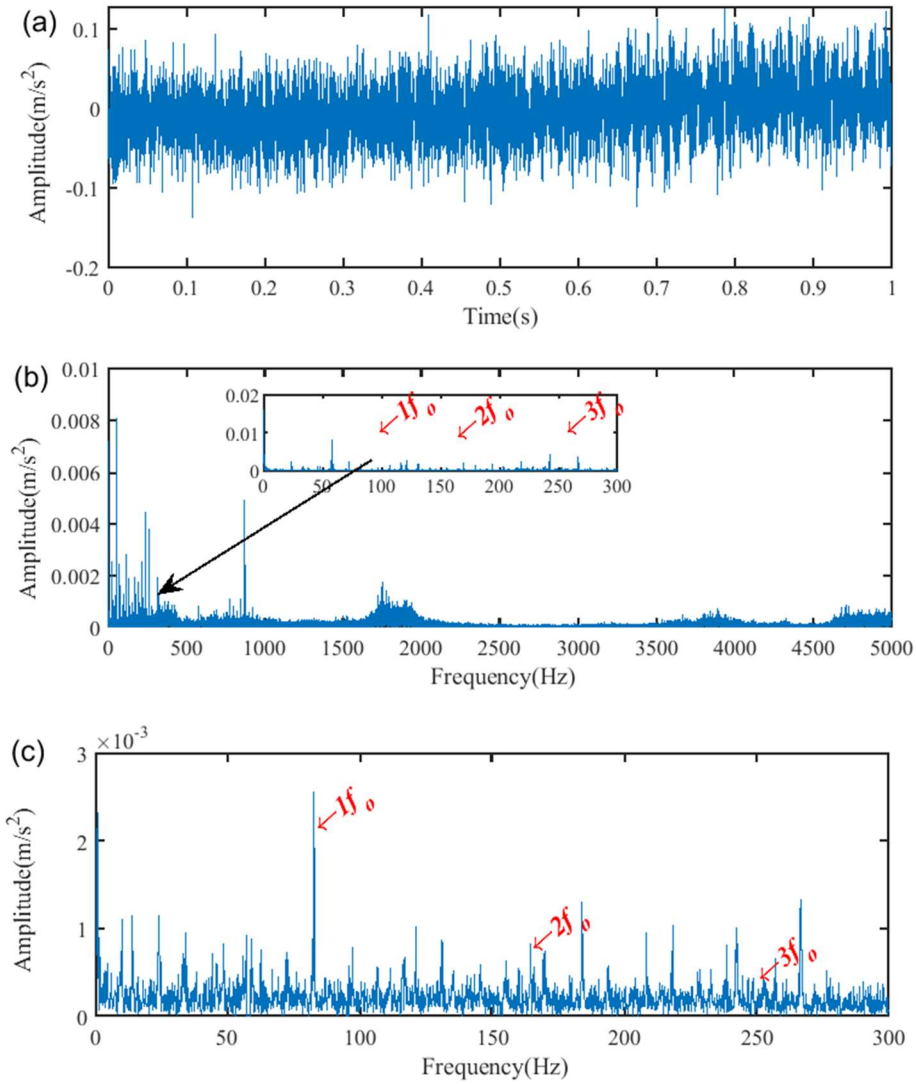


Fig. 24. Cylindrical roller bearing with outer race fault: (a) waveform; (b) spectrum; (c) envelope spectrum generated in the frequency band from 1600 Hz to 2000 Hz.

The iterative MDPW is then used to process the cylindrical roller bearing with outer race fault signal. First, the MDPW is implemented with a fixed flat SE with length of $L=5$ to deal with the measured signal. Then, the FSI of 50th iterations of MDPW are calculated by putting the number of MDPW iterations in order, and the maximum FSI value appears when $k=18$. Finally, the MDPW with 18th are utilized to handle the faulty bearing signal as shown in Fig. 24(a), and the process result is presented in Fig. 25. At the same time, there is no doubt that fault frequency f_o and its first 3 harmonics are visible in the Fig. 25(c).

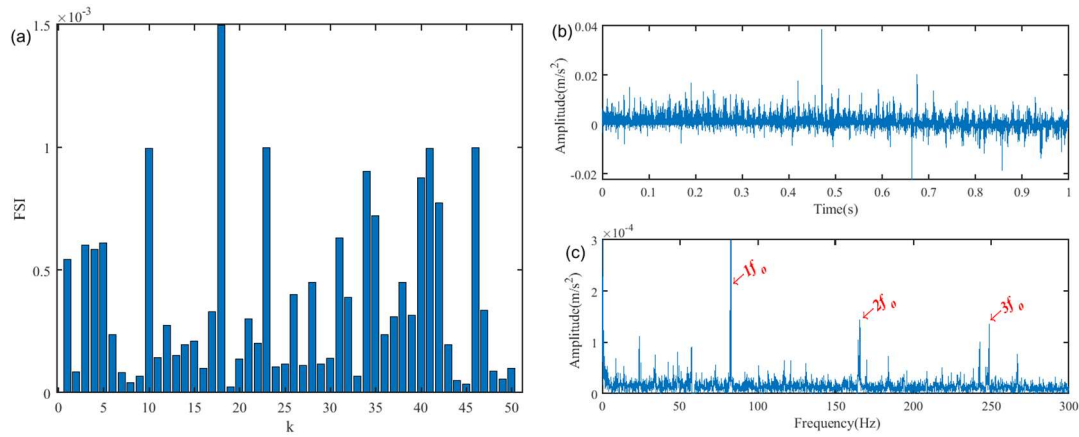


Fig. 25. Detection results of the iterative MDPW: (a) FSI value of MDPW (b) waveform (c) spectrum.

For comparison, the ASSMW and WSMW are used to process the defective bearing vibration signal as displayed in Fig. 24(a). Fig. 26 and Fig. 27 show the process results of the above two algorithms, respectively. In Fig. 26, the fault defect frequency f_0 and its harmonics are detected in the frequency spectrum, but a lot of unrelated frequency ingredients are more than that of MDPW as represented in Fig. 25. As depicted in Fig. 27, the magnitude of the fault frequency extracted by WSMW is significantly lower than that of the iterative MDPW. Besides, it has abundant background noise and interference frequencies at low frequencies. Therefore, the experimental results of the cylindrical roller bearing with outer race fault indicate that the iterative MDPW is more accurate for obtaining impulse features from residual noise and interference frequencies compared to other morphological filters (i.e., ASSMW and WSMW).

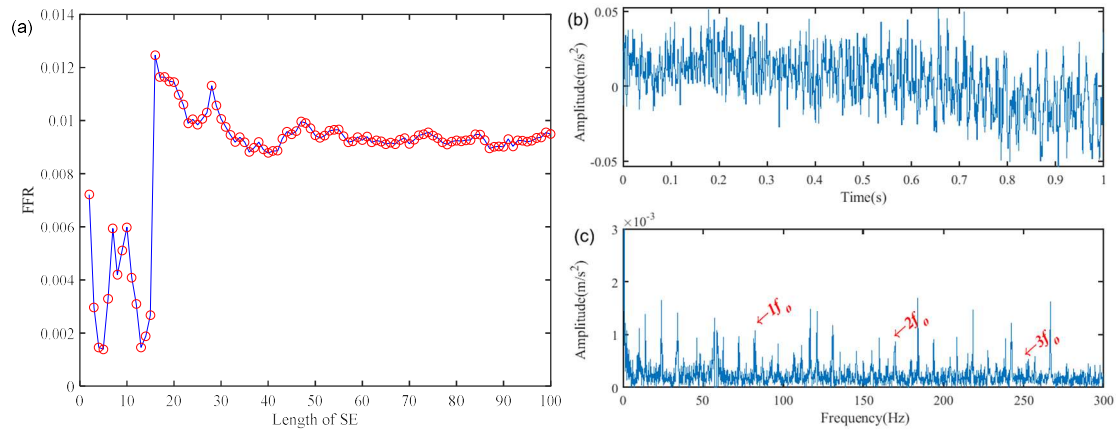


Fig. 26. Detection results of the ASSMW: (a) FFR value of ASSMW under different lengths of SE (b) waveform (c) spectrum.

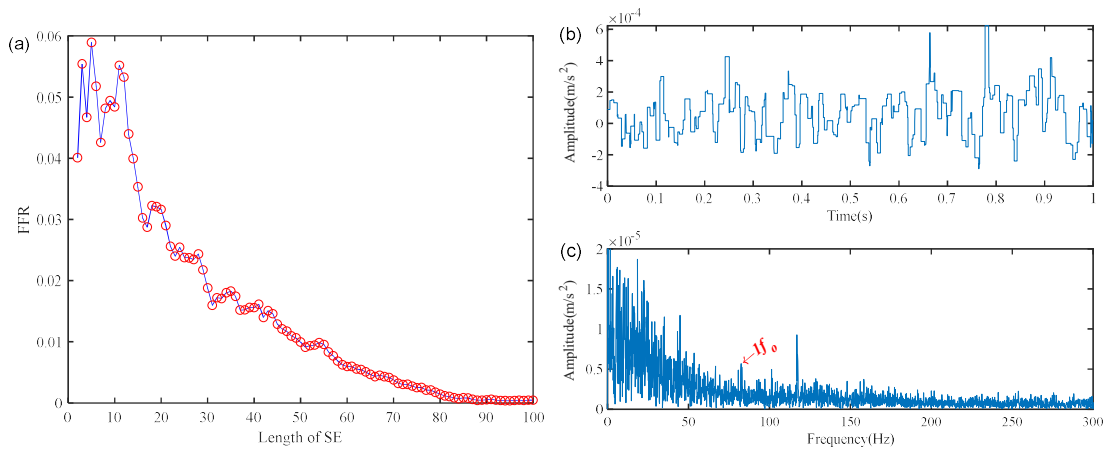


Fig. 27. Detection results of the WMSMW: (a) FFR value of WMSMW under different lengths of SE (b) waveform (c) spectrum.

In order to further assess the performance of iterative MDPW with FSI, the results are compared with ASSMW, WMSMW, iterative MDPW with GI and iterative MDPW with FFR. Fig. 28 presents the FI of the five methods for experimental case. As displayed in Fig. 28, the FI of iterative MDPW with FSI is higher than that of ASSMW, WMSMW, iterative MDPW with GI and iterative MDPW with FFR. In addition, the calculation cost of the three methods (e.g., iterative MDPW, ASSMW and WMSMW) are evaluated on a laptop computer. Fig. 29 presents the CPU time of iterative MDPW, ASSMW and WMSMW. As displayed in Fig. 29, the computational efficiency of iterative MDPW is higher than that of ASSMW and WMSMW. Consequently, the comparison results certificated that the fault diagnosis performance of iterative MDPW is superior to that of ASSMW and WMSMW.

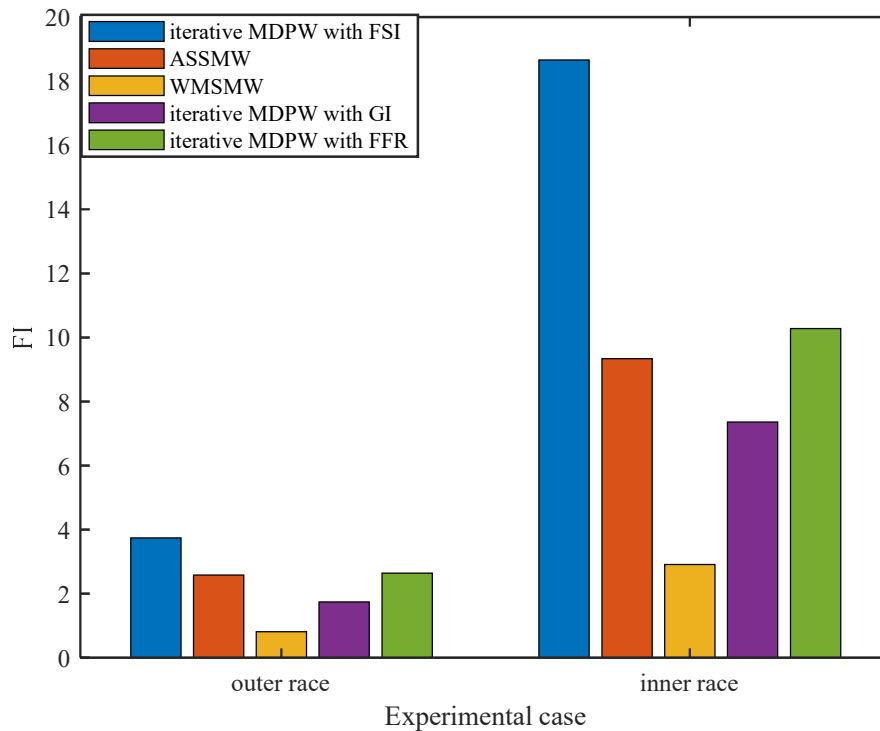


Fig. 28. FI of the five methods for experimental case.

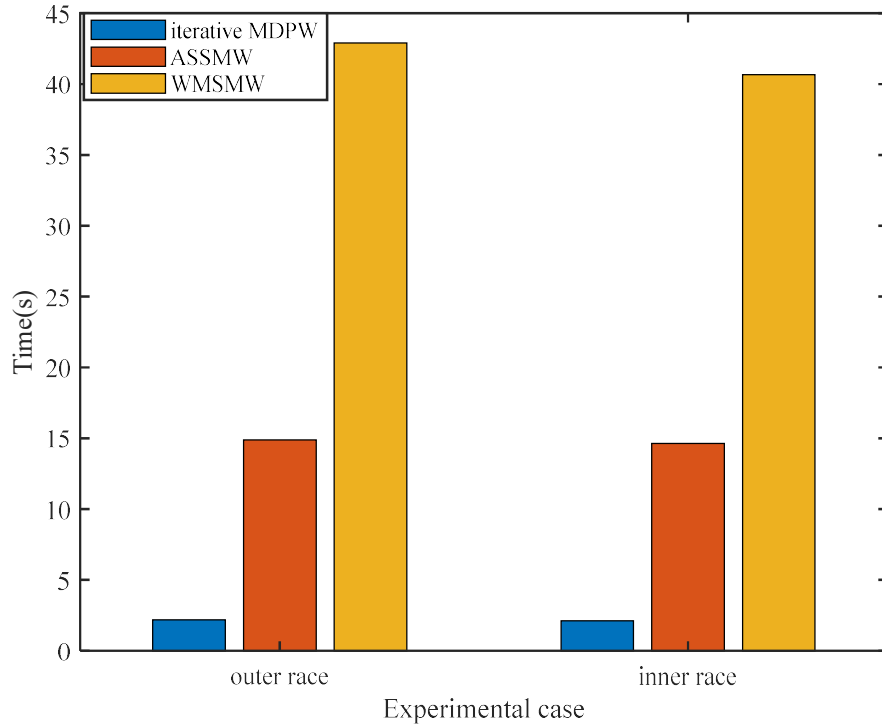


Fig. 29. Calculation time of three methods for experimental cases.

6. Conclusions

This work put forwards a weak feature extraction method using iterative MDPW for bearing fault diagnosis. For this method, an iterative criterion named FSI is proposed to obtain more fault components in the objective signal, which is based on the magnitude of the fault defect frequency and the GI index of the transient impulse. The primary advantages of the iterative MDPW are summarized as follows: (1) MDPW does not need to be usually determined by some complicated calculation formulas or empirical knowledge. (2) An iterative criterion FSI is put forward to select the optimal iterations number, which enhances the performance of MDPW in the weak fault extraction. (3) The iterative MDPW can effectively save the calculation cost. Simulation studies and experimental verification were performed to evaluate iterative MDPW by comparison with ASSMW and WMSMW. The results indicate that this paper provides a promising method for fault diagnosis and condition monitoring of rolling bearing. However, it is unidentified to us whether the iterative MDPW can be effectively applied to practical engineering. Thus, we will use the iterative MDPW to resolve kinds of complex practical engineering issues in future work.

Funding

This work was supported in part by the National Key Research and Development Program of China (Grant No. 2020YFB2007700), the National Science and Technology Major Project (Grant No. J2019-IV-0018-0086), the National Program for Support of Top-Notch Young Professionals, the China Postdoctoral Science Foundation (Grant No. 2021M702122), and the National Natural Science

Appendix. A

Initialization: Input the simulated bearing signal $x(t)$ and set the maximum MDPW iteration number $K=50$.

Repeat

for $k=1,2,\dots,K$ **do**

1) Conduct the four basic morphological operators to generate the combination morphological filter-hat transform ($A_{CO\&OC}H$) and difference filter ($G_{C\&O}$).

2) Obtain the morphological difference product filter (MDPF) through the combination of $A_{CO\&OC}H$ and $G_{C\&O}$.

3) Construct the MDPW by MDPF is incorporated into morphological undecimated wavelet (MUDW).

4) Implement the MDPW with a fixed SE length on the simulated bearing signal $x(t)$.

5) Calculate the FSI value for each iterative using Eq. (22).

end for

set $k=k+1$

until the termination condition is met

Output: Save the optimal MDPW iteration number and perform the MDPW with optimal iteration number to detect the fault defect frequencies from simulated bearing signal.

References

1. Jia F, Lei Y, Lu N, et al. Deep normalized convolutional neural network for imbalanced fault classification of machinery and its understanding via visualization. *Mech Syst Signal Pr*, 2018; 110: 349-367.
2. Jiang X, Wang J, Shen C, et al. An adaptive and efficient variational mode decomposition and its application for bearing fault diagnosis. *Struct Health Monit*, 2020; Epub ahead of print 25 November 2020. DOI: 10.1177/ 1475921720970856.
3. Wang D, Zhao X, Kou L, et al. A simple and fast guideline for generating enhanced/squared envelope spectra from spectral coherence for bearing fault diagnosis. *Mech Syst Signal Pr*, 2019; 122: 754-768.
4. Wang T, Chu F. Bearing fault diagnosis under time-varying rotational speed via the fault characteristic order (FCO) index based demodulation and the stepwise resampling in the fault phase angle (FPA) domain. *ISA Trans*, 2019; 94: 391-400.
5. Yunusa-Kaltungo A, Sinha JK Sensitivity analysis of higher order coherent spectra in machine faults diagnosis. *Struct Health Monit*, 2016; 15(5): 555-567.
6. Miao Y, Zhao M, Yi Y, et al. Application of sparsity-oriented VMD for gearbox fault diagnosis based on built-in encoder information. *ISA Trans*, 2020; 99: 496-504.
7. Dibag A, Eteffagh M, Hassannejad R, et al. Fine-tuned variational mode decomposition for fault

- diagnosis of rotary machinery. *Struct Health Monit*, 2019; 19(5): 1453-1470.
8. Yang H, Lin H, Ding K. Sliding window denoising K-singular value decomposition and its application on rolling bearing impact fault diagnosis. *J Sound Vib*, 2018; 421: 205-219.
 9. Zhang S, Lu S, He Q, et al. Time-varying singular value decomposition for periodic transient identification in bearing fault diagnosis. *J Sound Vib*, 2016; 379: 213-231.
 10. Li Y, Liang X, Xu M, et al. Early fault feature extraction of rolling bearing based on ICD and tunable Q-factor wavelet transform. *Mech Syst Signal Pr*, 2017; 86: 204-223.
 11. Pachori RB, Nishad A. Cross-terms reduction in the wigner-ville distribution using tunable-Q wavelet transform. *Signal Process*, 2016; 120: 288-304.
 12. Lei Y, Qiao Z, Xu X, et al. An underdamped stochastic resonance method with stable-state matching for incipient fault diagnosis of rolling element bearings. *Mech Syst Signal Pr*, 2017; 94: 148-164.
 13. He Q, Wu E, Pan Y. Multi-scale stochastic resonance spectrogram for fault diagnosis of rolling element bearings. *J Sound Vib*, 2018; 420: 174-184.
 14. Serra J, Vincent L. An overview of morphological filtering. *Circ Syst Signal Pr*, 1992; 11(1): 47-108.
 15. Ye Z, Yu J. Deep morphological convolutional network for feature learning of vibration signals and its applications to gearbox fault diagnosis. *Mech Syst Signal Pr*, 2021; 161: 107984.
 16. Luo J, Yu D, Liang M. Gear fault detection under time-varying rotating speed via joint application of multiscale chirplet path pursuit and multiscale morphology analysis. *Struct Health Monit*, 2012; 11(5): 526-537.
 17. Lv J, Yu J. Average combination difference morphological filters for fault feature extraction of bearing. *Mech Syst Signal Pr*, 2018; 100: 827-845.
 18. Guo J, Zhen D, Li H, et al. Fault detection for planetary gearbox based on an enhanced average filter and modulation signal bispectrum analysis. *ISA Trans*, 2020, 101: 408-420.
 19. Li Y, Zuo MJ, Chen Z, et al. Railway bearing and cardan shaft fault diagnosis via an improved morphological filter. *Struct Health Monit*, 2019; 19(5): 1471-1486.
 20. Li B, Zhang PL, Wang ZJ, et al. A weighted multi-scale morphological gradient filter for rolling element bearing fault detection. *ISA Trans*, 2011; 50(4): 599-608.
 21. Jiang W, Zheng Z, Zhu Y, et al. Demodulation for hydraulic pump fault signals based on local mean decomposition and improved adaptive multiscale morphology analysis. *Mech Syst Signal Pr*, 2015; 58-59: 179-205.
 22. Li C, Liang M, Zhang Y, et al. Multi-scale autocorrelation via morphological wavelet slices for rolling element bearing fault diagnosis. *Mech Syst Signal Pr*, 2012; 31: 428-446.
 23. Yan X, Jia M. Application of CSA-VMD and optimal scale morphological slice bispectrum in enhancing outer race fault detection of rolling element bearings. *Mech Syst Signal Pr*, 2019; 122:

56-86.

24. Deng F, Yang S, Tang G, et al. Self adaptive multi-scale morphology AVG-Hat filter and its application to fault feature extraction for wheel bearing. *Meas Sci Technol*, 2017; 28(4): 045011.
25. Guo J, Li H, Zhen D, et al. Transient impulses enhancement based on adaptive multi-scale improved differential filter and its application in rotating machines fault diagnosis. *ISA Trans*, 2021; Epub ahead of print 6 March 2021. DOI: 110.1016/j.isatra.2021.03.005.
26. Zhang J, Smith JS, Wu Q. Morphological undecimated wavelet decomposition for fault location on power transmission lines. *IEEE T Circ Syst*, 2006; 53(6): 1395-1402.
27. Goutsias J, Heijmans H. Nonlinear multiresolution signal decomposition schemes. Part 1: morphological pyramids. *IEEE T Image Process*, 9(11) (2000) 1862-1876.
28. Hao R, Chu F. Morphological undecimated wavelet decomposition for fault diagnostics of rolling element bearings. *J Sound Vib*, 2009; 320(4-5): 1164-1177.
29. Khakipour MH, Safavi AA, Setoodeh P. Bearing fault diagnosis with morphological gradient wavelet. *J Franklin I*, 2017; 354(6): 2465-2476.
30. Li B, Zhang PL, Mi SS, et al. An adaptive morphological gradient lifting wavelet for detecting bearing defects. *Mech Syst Signal Pr*, 2012; 29: 415-427.
31. Li Y, Liang X, Liu W, et al. Development of a morphological convolution operator for bearing fault detection. *J Sound Vib*, 2018; 421: 220-233.
32. Hu Z, Wang C, Zhu J, et al. Bearing fault diagnosis based on an improved morphological filter. *Measurement*, 2015; 80: 163-178.
33. Meng L, Xiang J, Wang Y, et al. A hybrid fault diagnosis method using morphological filter-translation invariant wavelet and improved ensemble empirical mode decomposition. *Mech Syst Signal Pr*, 2015; 50-51: 101-115.
34. Li Y, Zuo MJ, Lin J, et al. Fault detection method for railway wheel flat using an adaptive multiscale morphological filter. *Mech Syst Signal Pr*, 2017; 84: 642-658.
35. Yan X, Jia M, Zhang W, et al. Fault diagnosis of rolling element bearing using a new optimal scale morphology analysis method. *ISA Trans*, 2018; 73: 165-180.
36. Li Y, Zuo MJ, Xue Y, et al. An enhanced morphology gradient product wavelet for bearing fault detection. *Mech Syst Signal Pr*, 2017; 109: 166-184.
37. Xu X, Luo M, Tan Z, et al. Echo signal extraction method of laser radar based on improved singular value decomposition and wavelet threshold denoising. *Infrared Phys Techn*, 2018; 92: 327-335.
38. Wang Y, Xu G, Lin L, et al. Detection of weak transient signals based on wavelet packet transform and manifold learning for rolling element bearing fault diagnosis. *Mech Syst Signal Pr*, 2015; 54-55: 259-276.
39. Li C, Liang M. Continuous-scale mathematical morphology-based optimal scale band

- demodulation of impulsive feature for bearing defect diagnosis. *J Sound Vib*, 2012; 331(26): 5864-5879.
40. Hu A, Sun J, Xiang L. Analysis of morphological filter's frequency response characteristics in vibration signal processing. *Chin J Mech Eng*, 2012; 48(1): 98-103.
 41. Guo J, Shi Z, Zhen D, et al. Modulation signal bispectrum with optimized wavelet packet denoising for rolling bearing fault diagnosis. *Struct Health Monit*, 2021; Epub ahead of print 14 June 2021. DOI: 10.1177/14759217211018281.
 42. Wang D. Some further thoughts about spectral kurtosis, spectral L2/L1 norm, spectral smoothness index and spectral Gini index for characterizing repetitive transients. *Mech Syst Signal Pr*, 2018; 108: 360-368.
 43. Guo J, Zhang H, Zhen D, et al. An enhanced modulation signal bispectrum analysis for bearing fault detection based on non-Gaussian noise suppression. *Measurement*, 2020; 151: 107240.
 44. Tian X, Gu JX, Rehab I, et al. A robust detector for rolling element bearing condition monitoring based on the modulation signal bispectrum and its performance evaluation against the Kurtogram, *Mech Syst Signal Pr*, 2018; 100 (1): 167-187.